# Assessing the Regional Climate Response to Different Hengduan Mountains Geometries With a High-Resolution Regional Climate Model



**Author(s):**
Xiang, Ruolan; Steger, Christian R.; Li, Shuping; Pellissier, Loïc; Sørland, Silje Lund; Willett, Sean D.; Schär, Christoph

**Publication date:**
2024-03-28

**Permanent link:**
https://doi.org/10.3929/ethz-b-000666654



**Originally published in:**
Journal of Geophysical Research: Atmospheres 129(6), https://doi.org/10.1029/2023JD040208

JGR Atmospheres

RESEARCH ARTICLE
10.1029/2023JD040208

# Assessing the Regional Climate Response to Different Hengduan Mountains Geometries With a High-Resolution Regional Climate Model

**Ruolan Xiang[1], Christian R. Steger[1], Shuping Li[1,2], Loïc Pellissier[3], Silje Lund Sørland[1,4], Sean D. Willett[5], and Christoph Schär[1]**

[1]Institute for Atmospheric and Climate Science, ETH Zurich, Zurich, Switzerland, [2]College of Hydraulic Science and Engineering, Yangzhou University, Yangzhou, China, [3]Ecosystems and Landscape Evolution, Department of Environmental Systems Science, ETH Zurich, Zurich, Switzerland, [4]Sweco, Bergen, Norway, [5]Earth Surface Dynamics, Department of Earth Sciences, ETH Zurich, Zurich, Switzerland

**Abstract** The Hengduan Mountains (HM) are located on the southeastern edge of the Tibetan Plateau and feature high mountain ridges (>6,000 m MSL) separated by deep valleys. The HM region also features an exceptionally high biodiversity, believed to have emerged from the topography interacting with the climate. To investigate the role of the HM topography on regional climate, we conduct simulations with the regional climate model COSMO at high horizontal resolutions (at ∼12 km and a convection-permitting scale of ∼4.4 km) for the period 2001–2005. We conduct one control simulation with modern topography and two idealized experiments with modified topography, inspired by past geological processes that shaped the mountain range. In the first experiment, we reduce the HM's elevation by applying a spatially non-uniform scaling to the topography. The results show that, following the uplift of the HM, the local rainy season precipitation increases by ∼25%. Precipitation in Indochina and the Bay of Bengal (BoB) also intensifies. Additionally, the cyclonic circulation in the BoB extends eastward, indicating an intensification of the East Asian summer monsoon. In the second experiment, we remove deep valleys by applying an envelope topography to quantify the effects of terrain undulation with high amplitude and frequency on climate. On the western flanks of the HM, precipitation slightly increases, while the remaining fraction of the mountain range experiences ∼20% less precipitation. Simulations suggest an overall positive feedback between precipitation, erosion, and valley deepening for this region, which could have influenced the diversification of local organisms.

**Plain Language Summary** The Hengduan Mountains (HM), located on the southeastern edge of the Tibetan Plateau, feature high mountains separated by deep valleys. They also exhibit a particularly high biodiversity, which is believed to be caused by the interaction of mountain formation and climate. To understand the impact of HM geometry on local climate, we perform high-resolution atmospheric simulations with different HM shapes. We conduct one experiment with modern topography and two idealized experiments with modified topographies inspired by past geology: one where the mountains' elevation is lowered and another one where the deep valleys are filled. The first experiment reveals that the uplift of the HM leads to a local precipitation increase of ∼25%, with remote effects of enhanced precipitation in Indochina and the Bay of Bengal. The uplifted HM also makes the East Asia summer monsoon stronger. In the second experiment, when we remove the valleys, the western side of the mountains experiences a slight increase in precipitation, but the rest of the HM receives ∼20% less. This suggests that deep valleys amplify precipitation and accelerate erosion, further deepening these valleys over time. This positive feedback process could have supported the diversification of local organisms by offering a broader range of different climates.

**Key Points:**

- We perform high-resolution regional climate simulations over southeastern Tibet for contemporary climate and different mountain geometries
- The uplift of the Hengduan Mountains enhances local precipitation and amplifies summer monsoon circulation in East Asia
- Enhanced mountain relief leads to more precipitation, suggesting a positive feedback between precipitation and valley deepening by erosion

**Supporting Information:**

Supporting Information may be found in the online version of this article.

**Correspondence to:**

R. Xiang,
ruolan.xiang@env.ethz.ch

**Citation:**

Xiang, R., Steger, C. R., Li, S., Pellissier, L., Sørland, S. L., Willett, S. D., & Schär, C. (2024). Assessing the regional climate response to different Hengduan Mountains geometries with a high-resolution regional climate model. *Journal of Geophysical Research: Atmospheres*, *129*, e2023JD040208. https://doi.org/10.1029/2023JD040208

Received 18 OCT 2023
Accepted 4 MAR 2024

**Author Contributions:**

**Conceptualization:** Ruolan Xiang, Christian R. Steger, Shuping Li, Silje Lund Sørland, Christoph Schär
**Data curation:** Ruolan Xiang
**Formal analysis:** Ruolan Xiang, Christian R. Steger
**Funding acquisition:** Loïc Pellissier, Sean D. Willett, Christoph Schär
**Investigation:** Ruolan Xiang, Christian R. Steger, Christoph Schär
**Methodology:** Ruolan Xiang, Christian R. Steger, Shuping Li, Silje Lund Sørland, Sean D. Willett, Christoph Schär



## 1. Introduction

The Hengduan Mountains (HM) are located on the southeastern edge of the Tibetan Plateau (TP). Covering an area of over 600,000 km$^2$ and featuring an average elevation of more than 4,000 m MSL, the HM represents the longest and widest north-south mountain range system in China (Z. Li et al., 2011; Ning et al., 2012; K. Zhang et al., 2014). The contemporary topography is shaped by plate tectonics, which has led to the formation of folded mountains and a series of faulted basins, as well as by spatially heterogeneous erosion, responsible for the creation of deep river valleys. These valleys possess high topographic complexity and exhibit active geomorphic processes at the kilometer scale (Clark et al., 2005; L. Ding et al., 2022; Royden et al., 2008; Tian et al., 2015; E. Wang

**Supervision:** Christian R. Steger, Christoph Schär
**Validation:** Ruolan Xiang
**Visualization:** Ruolan Xiang, Christian R. Steger, Shuping Li, Loïc Pellissier
**Writing – original draft:** Ruolan Xiang, Christian R. Steger
**Writing – review & editing:** Christian R. Steger, Shuping Li, Loïc Pellissier, Silje Lund Sørland, Sean D. Willett, Christoph Schär

et al., 2012; Yang et al., 2016). Despite being located at higher latitudes, the HM hosts exceptionally high biodiversity, comparable to tropical regions (Mutke & Barthlott, 2005). This feature is believed to be linked to past complex interactions between plate tectonics, land surface dynamics, and atmospheric circulation in this region (Antonelli et al., 2018). Understanding the complex interaction between topography and climate is key to comprehending the features that make this region climatically and biologically unique.

Situated at the convergence of the Indian, East Asian, and western North Pacific summer monsoon systems (ISM, EASM, and WNPSM), the climate of HM exhibits a typical monsoon dynamic with distinct rainy and dry seasons (B. Wang & LinHo, 2002). The rainy season, which spans from May to September, sees the South Asian monsoon strike the mountain range, bringing substantial moisture and resulting in high rates of precipitation, particularly in the southwestern part of the HM (Z. Zhang et al., 2004). The influence of the north-south orientation of the HM is evident in the heterogeneous spatial distribution of local precipitation—the southwestern part of the HM receives relatively high precipitation, while the central and northeastern parts experience relatively low precipitation (Yu et al., 2018). Moreover, the complex topography with a profoundly dissected landscape generates a heterogeneous distribution of precipitation with a contrast between moist and dry valleys. Both the mean precipitation and precipitation extremes decrease from southwest to northeast across the HM (Z. Li et al., 2011; Ning et al., 2012; K. Zhang et al., 2014). Precipitation over the HM plays a significant role in shaping local ecological productivity through its impacts on glacier growth, surface runoff, and river flow (Dong et al., 2016; Qi et al., 2022).

The topography of the TP and the HM are known to significantly influence the Asian monsoon through both dynamic and thermal effects. The topography acts as a barrier, preventing the intrusion of cold, dry extratropical air into the warm, moist regions affected by the Asian monsoon (Boos & Kuang, 2010). Additionally, the landmass releases energy into the atmosphere in summer, inducing air pumping, deflecting mid-latitude westerlies, and generating cyclonic circulation in the lower troposphere in the Bay of Bengal (BoB) (Wu et al., 2012). However, the relative importance of these effects—i.e., the blocking versus air pumping—for monsoon formation remains a matter of debate (Acosta & Huber, 2020; G.-S. Chen et al., 2014; Molnar et al., 2010; Park et al., 2012; Xu et al., 2019).

Both data diagnosis and numerical experiments have exhibited that the topography affects the downstream EASM through mid-latitude Rossby wave propagation and air-sea interaction (KOSEKI et al., 2008; Duan et al., 2011; Y. Liu et al., 2020; M. Lu et al., 2023; Y. Zhang et al., 2004; Zhao & Chen, 2001). B. Wang et al. (2008) argued that the warming TP enhances summer frontal rainfall in the East Asia region by strengthening the anticyclonic circulation at upper levels and the cyclonic circulation at lower levels. This facilitates the eastward propagation of Rossby wave energy and fortifies the anticyclonic ridge over eastern China, strengthening moisture transport toward the East Asia subtropical front. According to Wu et al. (2017), under global warming, the sensible heat of the TP experienced a reduction from the mid-1970s to the end of the 20th century due to decreased surface wind speed. This reduction has resulted in a weakened near-surface cyclonic circulation and, consequently, a weakened EASM. Hence, the rain belt remains situated over South China, intensifying the precipitation in the region. The discrepancy between the findings of these studies may be ascribed to the different sources and uncertainties in data quality. A more reliable modeling study is required to tackle the physical processes by which the status of the TP affects the regional climate.

Numerical simulations have been widely employed to investigate the impact of mountain uplift on local and large-scale climate in interaction with the Asian monsoon system. Early studies focusing on the surface uplift effects of the TP treated the region as a single, vast feature, using low-resolution climate models with just two scenarios: with and without mountains (Manabe & Terpstra, 1974). Subsequent research used 'phased uplift' scenarios, assuming a linear increase in elevation based on the premise that past TP states can be approximated by spatially homogeneous scaling of contemporary topography (Botsyun et al., 2016; D. Jiang et al., 2008; X. Liu & Yin, 2002; Paeth et al., 2019). However, geological evidence suggests that the TP has experienced regional uplift, rather than a uniform rising process (Tapponnier et al., 2001). More realistic regional uplift scenarios are now being considered, and the role of the HM is being examined. H. Tang et al. (2013) found that the EASM enhancement is primarily driven by the surface sensible heating of the central and northern TP and HM. R. Zhang et al. (2015) underscored the role of the HM in modifying the low-level cyclonic circulation in the BoB, leading to substantial precipitation in this area. Yu et al. (2018) proposed that the uplift of the HM primarily causes local, rather than large-scale, changes. The topography in the HM is characterized by both the high average elevation and its local variance and both should be evaluated to understand the complex climate of the region.

The complex topography of the TP and HM regions poses a significant challenge to accurately modeling monsoon-influenced mountain climate. Yet, many previous terrain modification studies have relied on coarse-resolution global climate models, typically featuring a grid spacing of 100–200 km (Botsyun et al., 2016; D. Jiang et al., 2008; X. Liu & Yin, 2002; H. Tang et al., 2013; R. Zhang et al., 2015) or intermediate-resolution regional climate models with a grid spacing of 20–50 km (Paeth et al., 2019; Yu et al., 2018), which are unable to capture small-scale topography and its influence on the HM climate. Previous studies have demonstrated that high-resolution convection-permitting model (CPM) can offer a more accurate representation of climate, particularly in terms of capturing extreme events such as heavy precipitation and the water cycle in areas of complex terrain, compared to global climate simulations (Ban et al., 2015; Giorgi & Mearns, 1999; Kotlarski et al., 2014; Prein et al., 2016; Schiemann et al., 2014). Over the TP and the HM, Lin et al. (2018) found that CPM more effectively resolves orographic drag in complex terrains, enhancing the representation of water vapor transport and precipitation. Gao et al. (2020) emphasized the added value of CPM in accurately simulating the spatial distribution of precipitation and downstream snow simulation. P. Li et al. (2021) demonstrated that CPM more accurately depicts both the frequency and intensity of summer precipitation. Ma et al. (2022) observed that CPM yields better simulations of precipitation and temperature over the TP, notably improving the representation of the location and intensity of the heavy Meiyu precipitation. Z. Liu et al. (2022) showed that CPM more effectively captures the diurnal cycle of precipitation over the northern and eastern TP. However, due to high computational costs, previous studies utilizing CPMs over the TP and the HM have been constrained by short simulation periods or limited to small simulation domains.

In this study, we evaluate the impact of the HM geometry on both regional and local climates, with a focus on extreme precipitation events. We employ the regional climate model COSMO (Rockel et al., 2008) to conduct numerical experiments for the period from 2001 to 2005 with both contemporary and two idealized topographies that are linked to the formation of the HM. In the first experiment, we produce a topography with a lower average elevation in a spatially non-uniform way, which reflects a past potential state of the HM. In a second experiment, we eliminate deep valleys, formed by uplift and river incision, by applying an envelope topography to quantify their impact on climate. This experiment with smaller-scale terrain modifications focuses more on local-scale terrain influences on the atmosphere. For each topographic scenario, two distinct simulations are performed. The first simulation is performed with a grid spacing of 12 km. Subsequently, a higher-resolution simulation with a convection-permitting grid spacing of 4.4 km is nested within the first simulation.

The structure of the manuscript is as follows: Section 2 introduces the climate model used in this study and its configuration, the derivation of the idealized topographies, and the reference data employed in this study. Sect. 3 presents an evaluation of COSMO's capability to reproduce the control climate. Section 4 discusses the experiments with modified topography. Section 5 provides a summary of the main findings of this study and concluding remarks.

## 2. Methods and Data

### 2.1. Model Simulations

In this study, we apply the non-hydrostatic COSMO model (Rockel et al., 2008) in climate mode within a two-step, one-way nesting framework. The COSMO version used here takes advantage of a heterogeneous hardware architecture with Graphics Processing Units (GPUs), enabling more efficient exploitation of available hardware, and energy resources, and achieving higher computational performance (Fuhrer et al., 2014; Leutwyler et al., 2016). The model uses the generalized terrain-following height coordinate (Gal-Chen & Somerville, 1975) with rotated latitude-longitude coordinates and applies a split-explicit third-order Runge-Kutta scheme in time (Wicker & Skamarock, 2002). For convective parameterization, COSMO employs the Tiedtke Mass flux scheme with equilibrium closure based on moisture convergence (Tiedtke, 1989). The multi-layer soil model TERRA_ML, coupled with the groundwater-runoff scheme described by Schlemmer et al. (2018), is used for the representation of land surface processes (Heise et al., 2006). The radiation parameterization scheme is based on a $\delta$-two-stream version of the general equation for radiative transfer (Ritter & Geleyn, 1992). A turbulent-kinetic-energy-based parameterization is used for vertical turbulent diffusion and surface fluxes (Raschendorfer, 2001). Cloud microphysics is represented by a single-moment scheme that considers five species: cloud water, cloud ice, rain, snow, and graupel (Reinhardt & Seifert, 2006).

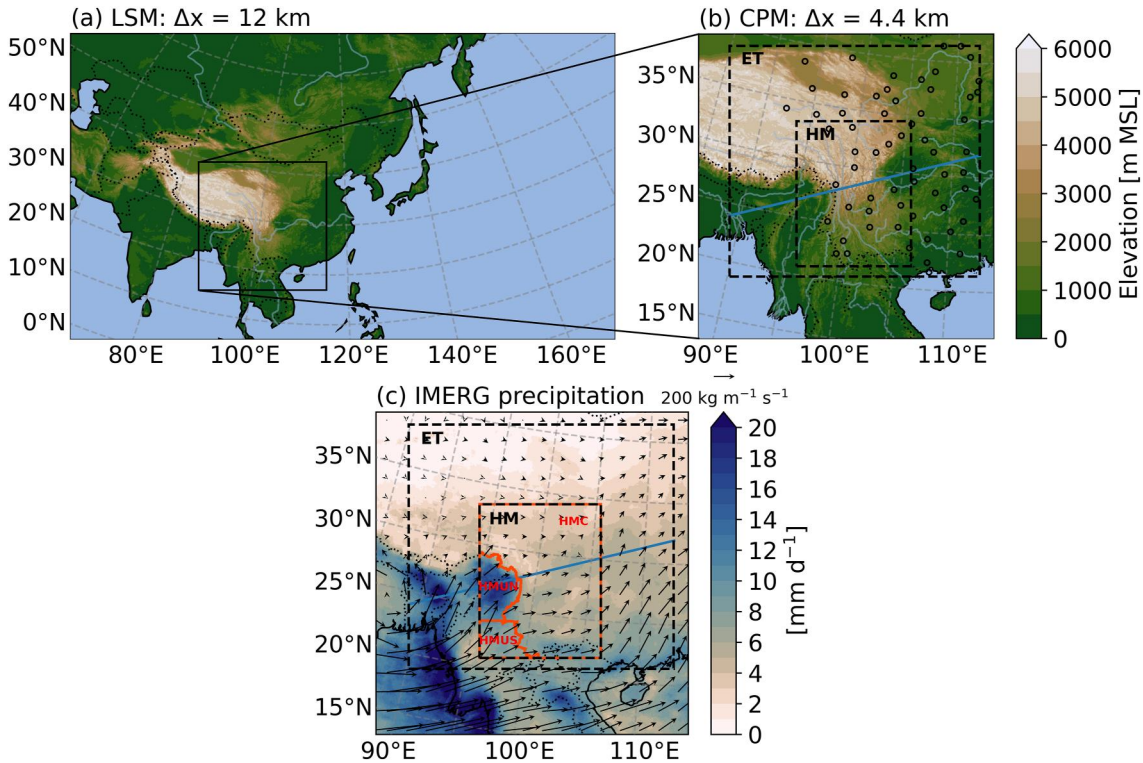


**Figure 1.** Overview of the COSMO domains used in this study. We apply (a) a large-scale domain at 12 km grid spacing (LSM) and (b) a nested domain at 4.4 km grid spacing (CPM). Black circles in (b) denote 62 precipitation stations in China considered for model evaluation. Additionally, the dashed outlines highlight the region of eastern Tibet (ET) and Hengduan Mountains (HM). In (b), the blue line represents a transect used in Section 4, which crosses the HM and is approximately parallel to the prevailing wind direction. Panel (c) shows the precipitation (units: mm $d^{-1}$) and vertically integrated water vapor transport (units: kg $m^{-1}$ $s^{-1}$) during the rainy season averaged over the year 2001–2005 from IMERG and ERA5, respectively. We further divide the HM into three subregions, including two upstream regions (HMUN, HMUS) with relatively high and low precipitation amounts, respectively, and one downstream region (HMC).

We use COSMO in the following framework: We define a large-scale model (LSM) domain (Figure 1a) with a grid spacing of 0.11° (~12 km) and 1,058 × 610 grid cells. This domain approximately corresponds to the CORDEX East Asia domain (Giorgi & Gutowski, 2015) but extends eastward to allow an unconstrained imprint of the modified topography on the large-scale climate downstream of the typical westerly flow. We perform LSM simulations with parameterized deep convection. Within the LSM domain, we nest a CPM with a grid spacing of 0.04° (~4.4 km) and 650 × 650 grid cells. The CPM domain, centered over the HM, covers Southwest China and parts of Indochina (Figure 1b). The CPM simulations explicitly resolve deep convection and are initialized from the LSM experiments. In the vertical direction, all simulations are run with 57 model levels ranging from the surface to the model top at approximately 30 km. We use a sponge layer with Rayleigh damping in the uppermost levels of the model domain. All simulations (control and two experiments with modified topography; see Section 2.2) span a 5-year period from 2001 to 2005. LSM simulations are initialized and laterally driven by the European Center for Medium-Range Weather Forecast (ECMWF) operational reanalysis ERA5 (Hersbach et al., 2020) at 6-hourly increments. Previous regional climate model experiments have shown that model performance can be improved with the application of spectral nudging (von Storch et al., 2000; Cha & Lee, 2009)—also for the East Asian region (D.-K. Lee & Cha, 2020; D. Lee et al., 2016; J. Tang et al., 2017). In this setup, forcings are stipulated not only at the lateral boundaries but also in large-scale flow conditions inside the model integration domain. However, we opt not to apply spectral nudging because modified topography is expected to impact climate on both local and larger scales. Spectral nudging would adjust large-scale atmospheric flow at upper levels toward the reanalysis state, which is derived from unmodified modern topography. To avoid this inconsistency and to allow for more unconstrained imprints of modified topography on large-scale flow, this technique is not used.

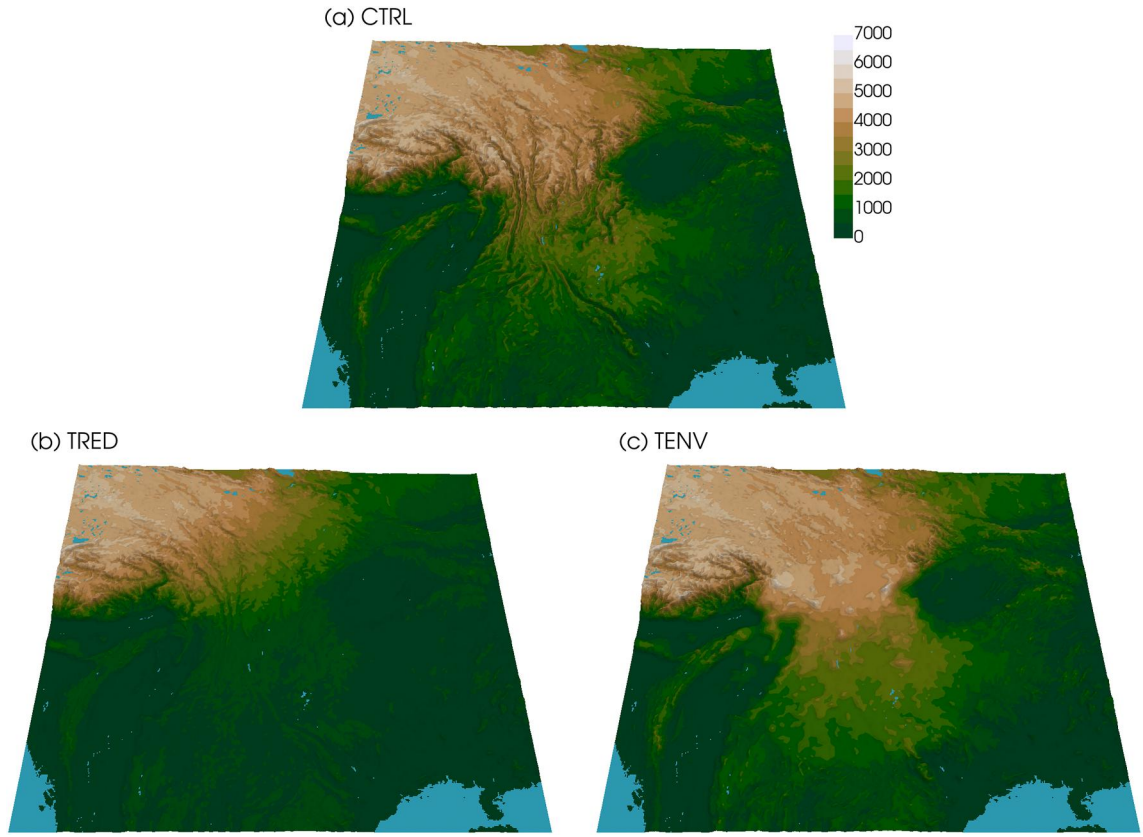


**Figure 2.** (a) Modern topography (CTRL), (b) reduced topography (TRED), and (c) envelope topography (TENV) in meters MSL at 4.4 km grid spacing.

### 2.2. Modification of the Hengduan Mountains' Topography

The modern control topography (Figure 2a), as well as the two modified topographies, are derived from the high-resolution digital elevation model (DEM) MERIT (Yamazaki et al., 2017). This DEM demonstrates very good performance in terms of data quality and general statistics compared to similar available DEM products for the High-Mountain Asia (HMA) region (K. Liu et al., 2019). For consistency, we apply the topographic changes to both the coarse- (0.11°/~12 km) and high-resolution (0.04°/~4.4 km) model topography. We refer to the coarse and high-resolution control simulations as CTRL11 and CTRL04, respectively. Before running COSMO simulations, we use COSMO's pre-processing tool EXTPAR (Asensio et al., 2021) to generate static external fields such as surface elevation, land-sea mask, and background albedo. Some of these fields, such as the orographic sub-grid parameters, depend on the raw input topography. To ensure consistency among all topography-based fields, we modify the MERIT data fed into EXTPAR, rather than altering the output topography from EXTPAR.

#### 2.2.1. Reduced Topography

To study the impact of regional surface uplift, we generate a topography representing a possible past stage of the HM with a lower average surface elevation. Detailed regional information on the past stages of the geological evolution of the Southeastern TP is uncertain (Royden et al., 2008). This hypothetical stage is inspired by the topographic configuration before the onset of the eastward extension in the central TP (Hoke et al., 2014). In this scenario, topographic changes are confined to the Southeastern TP and part of the Indochina Peninsula (Figure 2b). The east-west extension of the TP is represented in the model by a geographically-based modification of the modern HM topography, with elevation reductions ranging from 0% to 90%. A more detailed description of the topography modification scheme is presented in Supporting Information S1. We refer to the coarse-resolution simulation with reduced topography as TRED11 and the high-resolution simulation as TRED04.

**Table 1**
*Overview of the Applied Reference Data in This Study*

| Name | Type | Variables | Resolution (km) | Reference |
|---|---|---|---|---|
| ERA5 | Reanalysis | T, P, W, QV | ~30 | Hersbach et al. (2020) |
| APHRODITE | Ground in situ | P | ~25 | Yatagai et al. (2012) |
| AphroTemp | Ground in situ | T | ~25 | Yasutomi et al. (2011) |
| CRU | Ground in situ | T | ~50 | P. D. Jones et al. (2012) |
| IMERG | Remote sensing[a] | P | ~10 | Huffman et al. (2015) |
| GPCC | Ground in situ | P | ~50 | Schneider et al. (2014) |
| PBCOR | Combined[b] | P | ~5 | Beck et al. (2020) |
| CMA station | Ground in situ | P | – | CMA (2022) |

*Note*. For the applied variables: 2 m temperature (T), precipitation (P), wind (W) and specific humidity (QV) at 850 hPa. [a]Ground in situ data was used for calibration. [b]Inferred from reanalysis and ground in situ precipitation data, gridded evaporation data sets and observed runoff.

### 2.2.2. Envelope Topography

In this topography modification experiment, we investigate the role of deep valleys, which have formed through river incision and erosion, on the local climate. To remove river incisions from the modern topography, we compute an envelope topography. This concept has been applied in other studies (Li & Zhu, 1990; Damseaux et al., 2020), though driven by different research questions. We derive an envelope topography by computing a three-dimensional convex hull from the MERIT DEM, whose curvature is enhanced by a certain factor. The triangle mesh from the convex hull is subsequently rasterized back to the regular MERIT grid. This raw envelope topography is then embedded into the unmodified MERIT data with a 100 km wide transition zone to ensure smooth and continuous terrain between the raw envelope and the unmodified topography (see Figure S4c in Supporting Information S1). However, this embedded raw envelope topography represents an unrealistic scenario because the additional weight of the material used to fill the valleys would lead to an isostatic adjustment and, thus, a general lowering of the terrain. We account for this effect by estimating plate deflection using a two-dimensional model (Jha et al., 2017; Wickert, 2016). The final envelope topography that we apply is displayed in Figure 2c. A more detailed description of the topography modification scheme is presented in Text S2 in Supporting Information S1. We refer to the coarse-resolution simulation with envelope topography as TENV11 and the high-resolution simulation as TENV04.

### 2.2.3. Adjustment of Land Cover to Elevation Changes

Changes in the surface elevation of grid cells induce modifications in climate, such as temperature changes according to the local lapse rate. In turn, the local land cover would adjust to the new climate. A land cover type that is particularly sensitive to elevation is permanent ice (i.e., glacier coverage). Ice-covered grid cells exhibit distinctive surface properties (e.g., in terms of albedo) compared to unglaciated grid cells and should thus be adjusted in response to elevation changes. We perform a brief analysis of the regional line, above which permanent snow and ice prevail, based on GlobCover 2009 data (Arino et al., 2012). Based on these results, we adjust the glaciation of grid cells with changed elevation using a conservative approach (see Text S3 in Supporting Information S1). Additionally, in the case of a grid cell changing from ice-free to glaciated, there is a form of 'self-adjustment' in COSMO as such grid cells will accumulate permanent snow and will thus behave similarly to cells that are predefined as ice-covered. For other land cover classes, while their dependencies on elevation are recognized (Chang et al., 2023), they are complex and not yet fully understood in our study region. Adjusting

**Table 2**
*Precipitation Indices Applied in This Study*[a]

| Name | Definition | Units |
|---|---|---|
| Mean | Mean precipitation | mm $d^{-1}$ |
| Frequency | Wet day/hour frequency | – |
| Intensity | Wet day/hour intensity | mm $d^{-1}$ or mm $h^{-1}$ |
| pxD | The *x*th percentile of daily precipitation | mm $d^{-1}$ |
| pxH | The *x*th percentile of hourly precipitation | mm $h^{-1}$ |

[a]Note that all percentile indices are expressed relative to all (wet and dry) days/hours (Schär et al., 2016).

these classes without solid scientific grounding could introduce further uncertainties and biases into the model. Moreover, the differences between vegetation classes (e.g., in terms of albedo) are generally less pronounced than those between ice-covered and non-glaciated grid cells. Therefore, we have opted to retain the original land cover classes, with the exception of the ice class.

### 2.3. Reference Data

To evaluate the model's performance, we employ a combination of in situ observations, satellite products, and reanalysis data (see Table 1 for an overview and product references). ERA5 reanalysis data are used to evaluate the large-scale circulation simulated by COSMO, as well as 2 m air temperature and precipitation. In evaluating precipitation, we additionally consider the following observation-based products: Integrated Multi-satellite Retrievals for Global Precipitation Measurement (IMERG), the Asian Precipitation—Highly-Resolved Observational Data Integration Toward Evaluation (APHRODITE), and the Global Precipitation Climatology Center (GPCC) data set. The first product is derived from remote sensing information and calibrated with ground in situ data, while the latter two data sets are inferred from precipitation gauge measurements only. Gauge-derived or calibrated gridded precipitation data sets tend to underestimate actual precipitation (Prein & Gobiet, 2017; Singh & Kumar, 1997), particularly in areas with complex terrain and at higher latitudes (Beck et al., 2020). Such biases are also quantified for our study region (Y. Jiang et al., 2022) and are primarily caused by two factors: first, rain gauges undercatch precipitation, particularly in wind-exposed and snow-dominated environments (Kirschbaum et al., 2017; Schneider et al., 2014). Second, precipitation gauge networks are disproportionately located in valley floors, which typically receive less precipitation than valley flanks and ridges (Rasmussen et al., 2012; Sevruk et al., 2009). GPCC is corrected for precipitation undercatch (Schneider et al., 2014) but not for the second issue mentioned above. Therefore, we consider another precipitation reference product (called PBCOR) from Beck et al. (2020). This product accounts for both undercatch and the spatial non-representativeness of gauge stations by estimating precipitation as a residual from modeled/observed evaporation and runoff. The output from this study has been applied in Prein et al. (2022) to evaluate modeled precipitation in the HMA region. Moreover, we consider hourly precipitation measurements from 62 ground-based meteorological stations of the China Meteorological Administration (CMA; see Figure 1b for station locations) to compare the impact of parameterized versus explicitly represented deep convection on modeled precipitation. We use the method outlined by Kaufmann (2008) to compare modeled precipitation with station data. For CTRL11, the station data are compared with values from the closest model grid cell. For CTRL04, we select the grid cell closest to the station's altitude within a 6 km radius. This method has previously been utilized by Ban et al. (2015) and S. Li et al. (2023) in their validation of simulated precipitation against station data. To further assess the 2 m air temperature, we consider two station-derived products: the APHRODITE daily mean temperature data set (AphroTemp), and the surface observation time-series data set from the University of East Anglia Climatic Research Unit (CRU).

### 2.4. Precipitation Indices and Spatiotemporal Evaluation

We use multiple statistical indices outlined in Table 2 to study the characteristics and variations of precipitation and its extremes in both observational data and model simulations. Following Ban et al. (2021), a wet day is defined as daily precipitation greater than or equal to 1 mm $d^{-1}$, and a wet hour is defined as hourly precipitation greater than or equal to 0.1 mm $hr^{-1}$.

For the majority of our analyses, we consider the rainy (MJJAS) and dry (NDJFM) seasons, which are common periods for studying Asian monsoon climate (B. Wang, 2006; B. Wang & LinHo, 2002). We mostly focus on the summer monsoon (MJJAS), because the majority of the yearly accumulated precipitation occurs in this period in the HM and the surrounding area. In the validation part (Section 3) however, we also carry out model evaluations on a seasonal basis, that is, for winter (DJF), spring (MAM), summer (JJA), and autumn (SON) over 5 years, to allow for a direct comparison with previous modeling studies (e.g., B. Huang et al. (2015); W. Zhou et al. (2016)).

For spatial analysis, we define multiple domains, which are displayed in Figures 1b and 1c. The largest domain, ET, encompasses the majority of the land area of the CPM domain and all CMA precipitation gauge stations (see

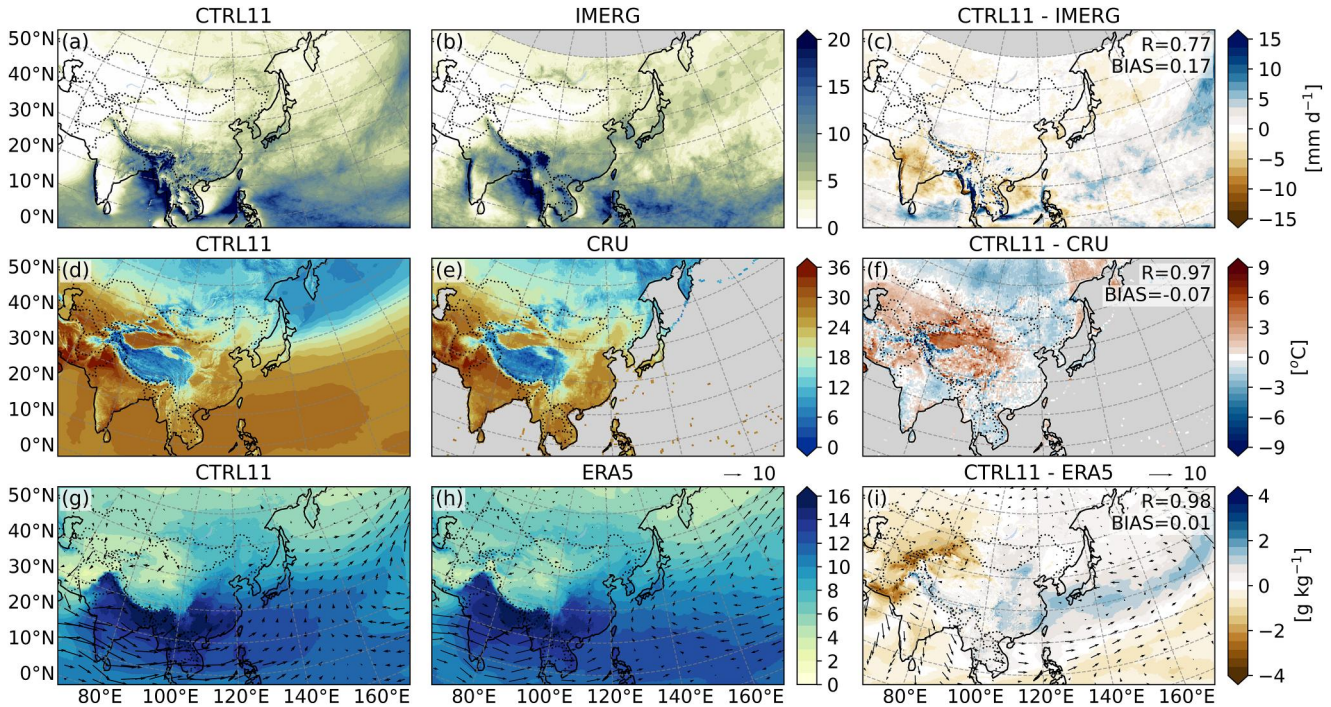


**Figure 3.** Spatial distributions of JJA (a–c) precipitation (units: mm $d^{-1}$), (d–f) 2 m air temperature (units: °C) and (g–i) 850-hPa wind (vector; units: m $s^{-1}$) and specific humidity (shading; units: g $kg^{-1}$). All quantities are averaged over the period 2001–2005. The first column displays the CTRL11 model, the second one observations and the third one their differences. Correlation coefficients and spatially integrated biases are indicated in the upper-right part of panels (c), (f) and (i) for precipitation, 2 m air temperature and specific humidity, respectively. Missing values in IMERG and CRU are represented by gray areas.

Figure 1b). The HM domain contains the majority of the area that is affected by the topographic modification scenarios (see Section 2.2). We further split this domain according to the national boundaries between China and India/Myanmar into an upstream and a center region (HMU and HMC, respectively). HMU represents the HM area that is located upstream of the prevailing atmospheric flow during the summer monsoon (see Figure 1c). For model evaluation (see Section 3.2), this domain is divided again into a northern part (HMUN), which experiences very large precipitation amounts, and a southern part (HMUS) which features a dryer climate.

## 3. Evaluation of Simulated Climate Over 2001–2005

In this section, we first validate the ability of the coarser-scale, CTRL11 simulation to reproduce the characteristics of the East Asian summer climate. We conduct an evaluation of this simulation for each season independently. To keep this section concise, we present only the results for the summer season, with those for winter, spring, and autumn available in Figures S6–S11 in Supporting Information S1 for a more comprehensive view. Subsequently, we evaluate the convection-permitting control simulation CTRL04. This evaluation places a focus on extreme precipitation indices, for which we use an extended set of rain gauge precipitation stations in China that operate at an hourly resolution.

### 3.1. East Asian Climate

The performance of CTRL11 in simulating the mean characteristics of the East Asian summer climate is presented in Figure 3. We remap the model outputs to the corresponding observation or reanalysis grids using bilinear interpolation for continuous variables like temperature and wind speed. Precipitation is remapped using the first-order conservative method to maintain the water budgets (P. W. Jones, 1999). Figures 3a–3c display the mean precipitation from June to August during 2001–2005 in CTRL11, IMERG, and their difference. The spatial distribution of summer precipitation over East Asia shows significant variation, and CTRL11 simulation reproduces these variations quite well with a pattern correlation of 0.77 and a mean bias of 0.17 mm $d^{-1}$. However, it is important to note the presence of compensation effects. During the summer season, areas near the southern coast of the continent, including the northeastern BoB, the northeastern Arabian Sea, the Philippine Sea, and the

South China Sea (SCS), experience the highest precipitation amounts in both the simulation and the observation. The southern flanks of the Himalayas also receive heavy rainfall due to the monsoon winds bringing moisture from the Indian Ocean and the BoB—a process effectively captured by our model. However, the summer precipitation over India and the SCS is underestimated in CTRL11 by 3–5 mm $d^{-1}$ (Figure 3c). In contrast, in the mid-latitude regions of the West Pacific Ocean and the low-latitude region of the BoB, the precipitation is overestimated by approximately 5 mm $d^{-1}$. The precipitation bias pattern over the lower latitudes in CTRL11 resembles that found in previous modeling studies over this area (B. Huang et al., 2015; W. Zhou et al., 2016). Unlike previous modeling efforts (Bucchignani et al., 2014; D. Wang et al., 2013), our simulations feature lower precipitation biases over the TP, indicating potential benefits from employing a higher spatial resolution.

Figures 3d–3f illustrate the simulated and observed mean summer 2 m air temperature and the difference between the simulation and the CRU data set. CTRL11 reproduces the observed spatial pattern of surface air temperature very accurately, with a pattern correlation of 0.97. A weak cold bias is present over Siberia, while central Asia exhibits an evident warm bias. W. Zhou et al. (2016) reported a similar warm bias during the summer season in their COSMO simulations. In CTRL11, the simulated surface air temperature aligns better with observations over India, the Indochina peninsula, TP, and southeastern China compared with previous simulations (Bucchignani et al., 2014; Meng et al., 2018; W. Zhou et al., 2016).

To understand the biases in surface climatology, we compare the low-level atmospheric flow and specific humidity between CTRL11 and the ERA5 reanalysis data. Figures 3g–3i depict the spatial patterns of the wind and specific humidity at 850 hPa. The specific humidity reveals excellent spatial agreement with the reanalysis, demonstrating a pattern correlation of 0.98 and a bias of 0.01 g $kg^{-1}$. The most significant negative biases in specific humidity occur over Central Asia and Pakistan. CTRL11 simulates a stronger northerly flow over Afghanistan and Pakistan. This flow correlates with the transportation of drier continental air toward the coastal regions, which then advects over India, potentially causing the precipitation bias there.

The region of Asia experiencing the monsoon weather pattern exhibits the most distinct annual variations in precipitation, characterized by alternating dry and wet seasons synchronized with the seasonal reversal of the monsoon circulation features (Webster et al., 1998). The monsoon circulation patterns in India and East Asia have unique characteristics (Y. Ding & Chan, 2005). Figure 4 presents a Hovmöller diagram of the observed and simulated annual cycle of meridional precipitation (from 5°N to 50°N, and zonally averaged over 70–80°E and 110–120°E). The ISM's and EASM's spatiotemporal characteristics are very well captured in this representation. It shows a generally good alignment between CTRL11 and IMERG, particularly in terms of the temporal and latitudinal progression of monsoon precipitation. CTRL11 effectively captures the gradual onset of the monsoon over India, but it does underestimate rainfall during the summer season (Figure 4a). As shown in Figure 4b, before mid-May, the main rain belt in the SCS longitudes is located south of 10°N, while a second rain belt is found in South China between 20 and 30°N. Around mid-May, the tropical rain belt suddenly shifts northward, resulting in the merging of the two rain belts. CTRL11 accurately captures this rapid onset process, which has also been documented by previous monsoon studies (Y. Ding & Chan, 2005; Matsumoto, 1997; B. Wang & LinHo, 2002).

### 3.2. Eastern Tibet Climate

We evaluate the accuracy of the simulated ET and HM climate by comparing it with several observational data sets. Figure 5a displays the ET-averaged seasonal precipitation cycle based on observational data, reanalysis, and model simulations. The seasonal cycle of precipitation over ET typically features a dry winter and a prolonged rainy season from May to September, with a precipitation peak in July, according to the reference data. In terms of precipitation magnitudes, both CTRL11 and CTRL04 closely match or fall within the upper bound of the reference data sets. However, it's important to note that the APHRODITE data set does not correct for any orographic effects discussed in Section 2.3. The GPCC data set, which is partially corrected, aligns better with the simulated precipitation values. The closest agreement is with PBCOR, which takes into account undercatch effects, and ERA5, a model-based data set that does not have the limitations stated in Section 2.3. A study by Y. Jiang et al. (2022) conducted for a sub-region of the ET domain, found that simulation-based precipitation data sets (e.g., ERA5) perform better than IMERG in terms of precipitation intensity. The seasonal precipitation cycle is well captured by both CTRL11 and CTRL04, although both simulations show an earlier onset of monsoon precipitation, with the annual maximum precipitation occurring in June. This bias likely stems from an early development of the summer monsoon circulation, represented by a lower-level westerly atmospheric flow, in our

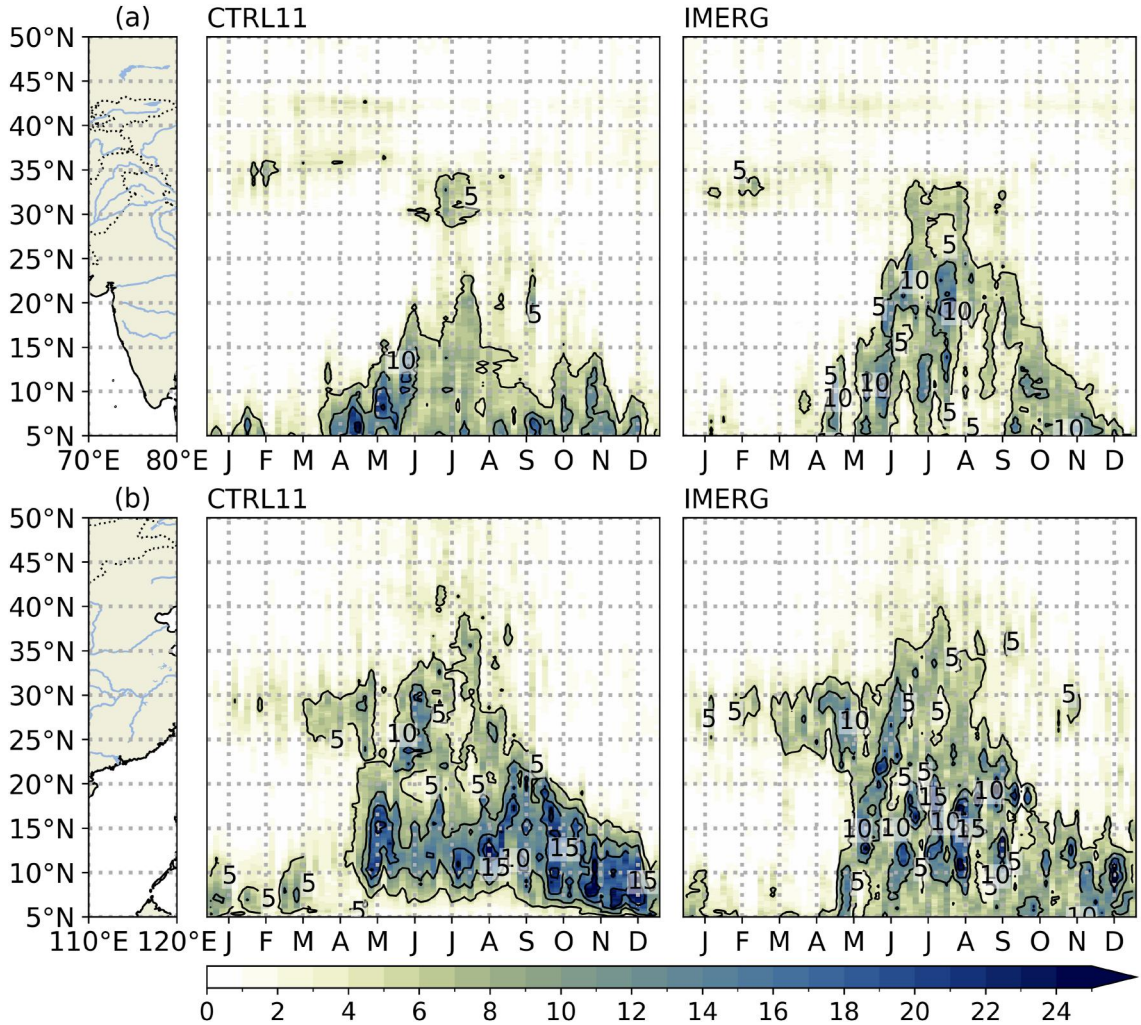


**Figure 4.** Hovmöller diagrams of the seasonal precipitation cycle zonally averaged over (a) 70–80°E and (b) 110–120°E (units: mm $d^{-1}$). A 5-day moving average has been applied to the 5-year climatology to remove high-frequency variability.

simulations. A study by D. Lee et al. (2016), in which COSMO was applied for East Asia, also identified an unseasonably early precipitation peak, demonstrating that improved alignment could be achieved through spectral nudging. Our analyses of the seasonal precipitation cycles for the sub-regions of ET yielded similar results to those shown in Figure 5a, so we present only the condensed results for the rainy/dry seasons and the annual averages in Figure 5b. Our simulations effectively capture the spatially different precipitation magnitudes, such as the very high summer monsoon precipitation in the HMUN region, aligning well with ERA5 and PBCOR. Both CTRL11 and CTRL04 generally overestimate precipitation in the dry season, which is likely due to the premature onset of the summer monsoon in our simulations.

Figure 5c presents our analysis of the mean seasonal cycle of 2 m temperature. Compared to the station-derived data sets and ERA5, CTRL11 exhibits a weak warm bias, while CTRL04 aligns better with the reference data sets. The model's performance across both the rainy and dry seasons shows high consistency. The HM region, as well as the ET domain, feature complex terrain that ranges from sea level to approximately 7,000 m. Figure 5d shows how well 2 m temperatures, as a function of elevation, are represented in our control experiments. The agreement with APHRO_Temp and CRU is excellent for both seasons but seems to deteriorate slightly at higher elevations. This might be due to the typically larger uncertainty of the reference products at higher elevations, given the sparser station coverage. Notably, CTRL04 and CTRL11 align much better with APHRO_Temp and CRU at higher elevations in the dry season compared to ERA5, which tends to underestimate temperature. This underestimation in

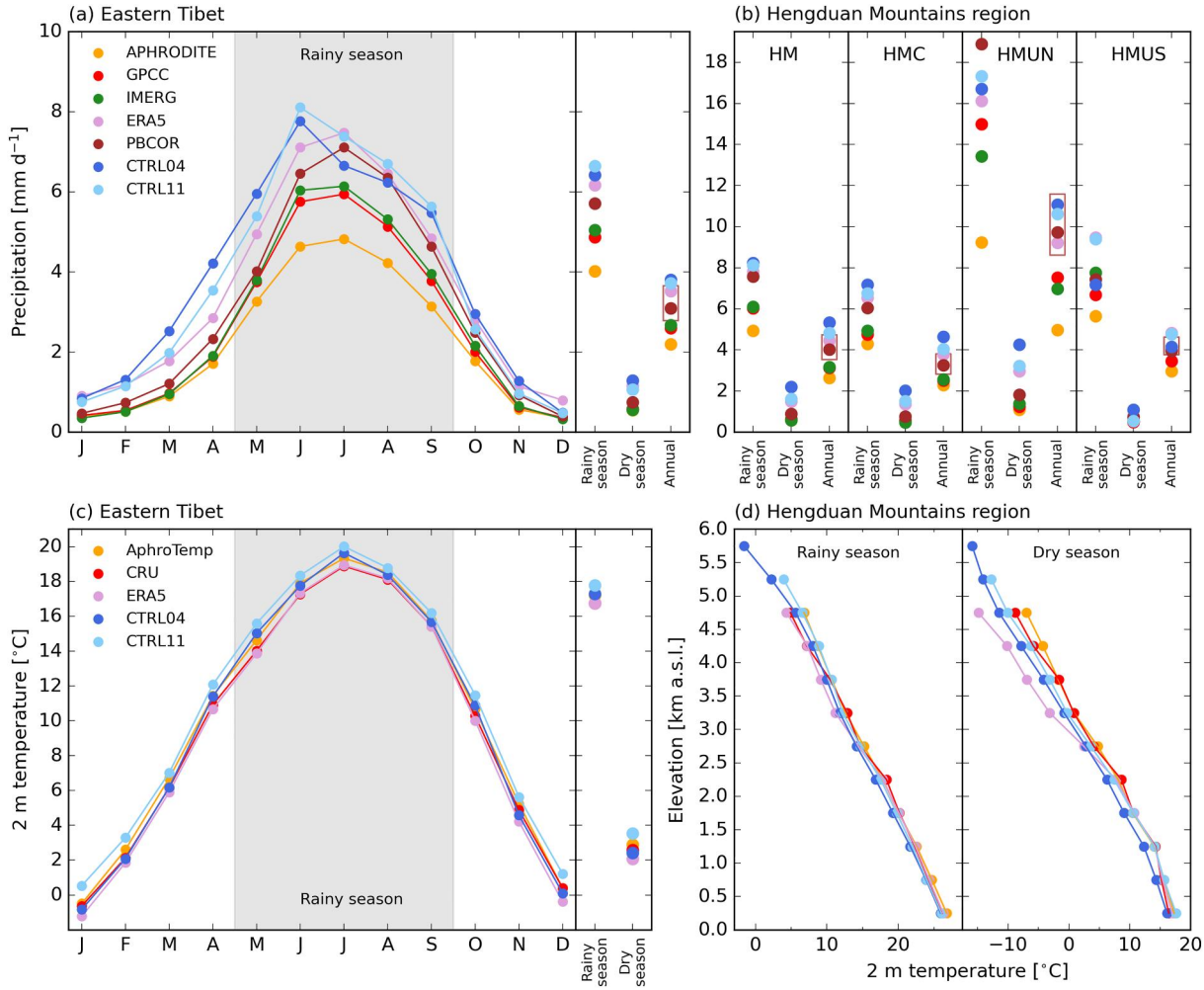


**Figure 5.** Seasonal cycles of (a) precipitation and (c) 2 m temperature of control simulations and the reference data sets averaged over the Eastern Tibet domain. Temporally integrated quantities over the rainy (MJJAS) and dry (NDJFM) seasons (and the entire year) are displayed on the right. Panel (b) shows precipitation for the rainy/day season and averaged over the year for the Hengduan mountains sub-regions. Note the different y-axis range. The brown boxes in panel (a) and panel (b) specify the uncertainty range of PBCOR for the annual values. Panel (d) displays the 2 m temperature as a function of elevation for the rainy and dry seasons integrated over the HM region.

ERA5 relates to the overestimation of snow coverage in ERA5 in the HMA region (Orsolini et al., 2019). In contrast, snow coverage in our simulations aligns well with observational data sets (not shown).

To further explore the impact of explicitly resolved convection on simulated precipitation, we perform a validation using data from 62 rain gauge stations across the ET that recorded hourly measurements during the simulation period. Figure 6a illustrates the comparison of observed and modeled wet-day frequency. We found that CTRL11 tends to over-represent drizzle events, with a bias of 6.86%. In contrast, CTRL04 aligns more closely with the observed data, with a bias of −0.23%. Regarding wet-day intensity, CTRL04 tends to overestimate daily precipitation, presenting a bias of 3.35 mm d$^{-1}$ (Figure 6b). However, it's important to note that rain gauges are subject to precipitation undercatch issues, likely leading to observed intensities that are too small. Conversely, CTRL11 tends to underestimate daily precipitation intensity, a tendency also noted in other geographical regions (e.g., Ban et al. (2021)). Figure 6c demonstrates that CTRL04 slightly underestimates the wet-hour frequency (bias = −0.45%), while CTRL11 tends to overestimate it (bias = 4.74%). This issue of excessive drizzle in CTRL11 is a common challenge in many climate models (D. Chen et al., 2021; Stephens et al., 2010; Trenberth & Zhang, 2018). However, the enhanced convection representation in CTRL04 effectively alleviates this drizzling problem, which is consistent with a previous study by P. Li et al. (2021). In terms of simulating hourly precipitation, CTRL04 provides a more accurate representation of intensity than CTRL11, as

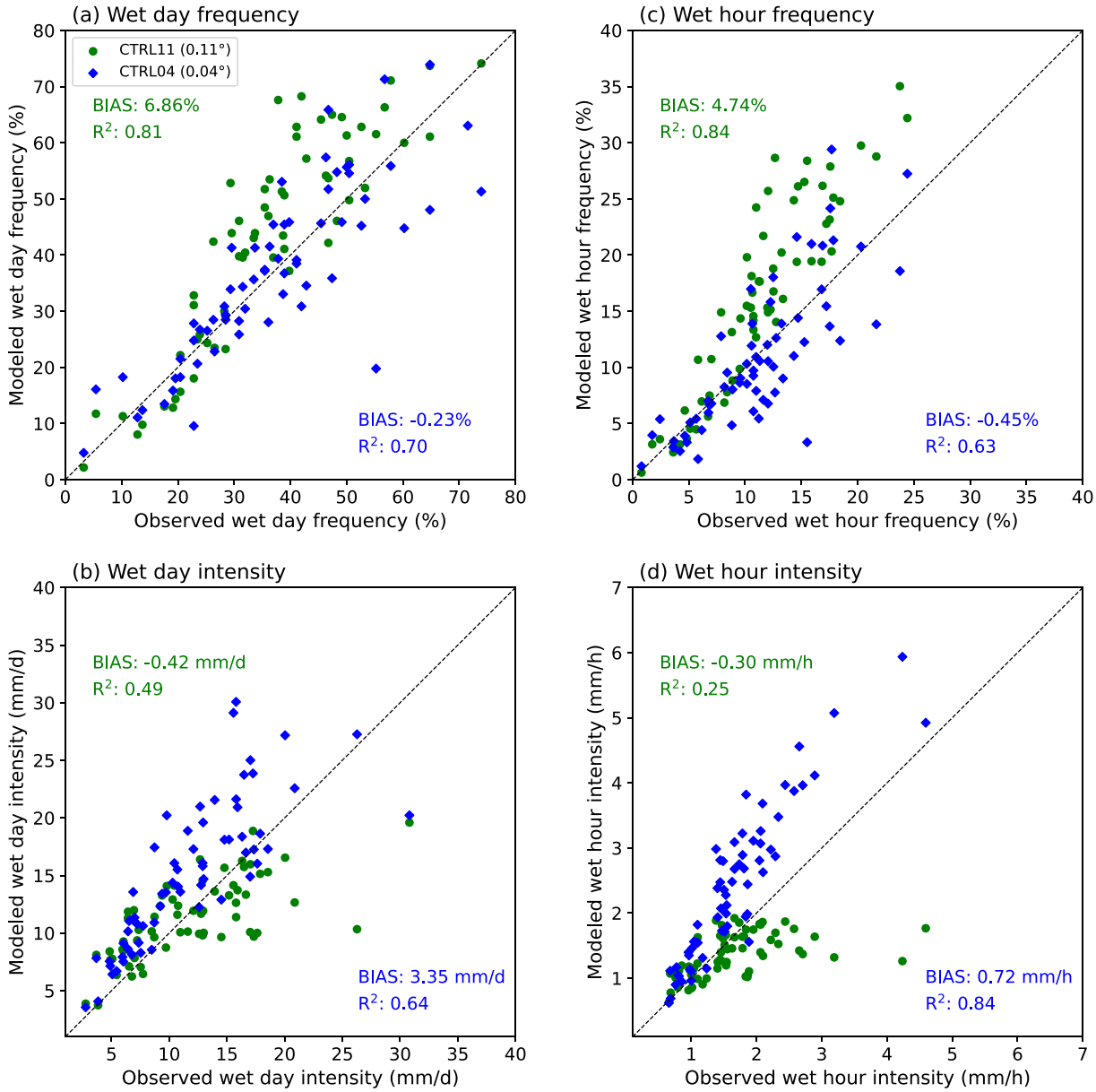


**Figure 6.** Validation of JJA precipitation for ERA5-driven simulation with 12 km (CTRL11, green) and 4.4 km (CTRL04, blue) grid spacing with in situ precipitation data from 64 stations in China: (a) wet day frequency (units: %), (b) wet day intensity (units: mm $d^{-1}$), (c) wet hour frequency (units: %), and (d) wet hour intensity (units: mm $h^{-1}$). $R^2$ denotes the square of the correlation coefficient between the models and observations.

shown in Figure 6d. CTRL11 tends to significantly underestimate wet-hour intensity, particularly at stations where heavy hourly precipitation occurs, consistent with previous studies (S. Li et al., 2023; Schär et al., 2020; Zeman et al., 2021). For locations with high hourly intensities, CTRL11 underestimates precipitation intensity by up to a factor of 3 ($R^2$ = 0.25)—a difference that can be essential for erosion and river runoff (Nearing et al., 2005). Overall, the model evaluation with in situ rain gauge station data suggests that high-resolution convection-permitting simulations deliver better performance in reproducing precipitation indices in this region. Consequently, the explicit representation of convection and the finer spatial grid at 4.4 km appear beneficial for simulating precipitation characteristics in our domain, which features complex terrain and a monsoon-dominated climate.

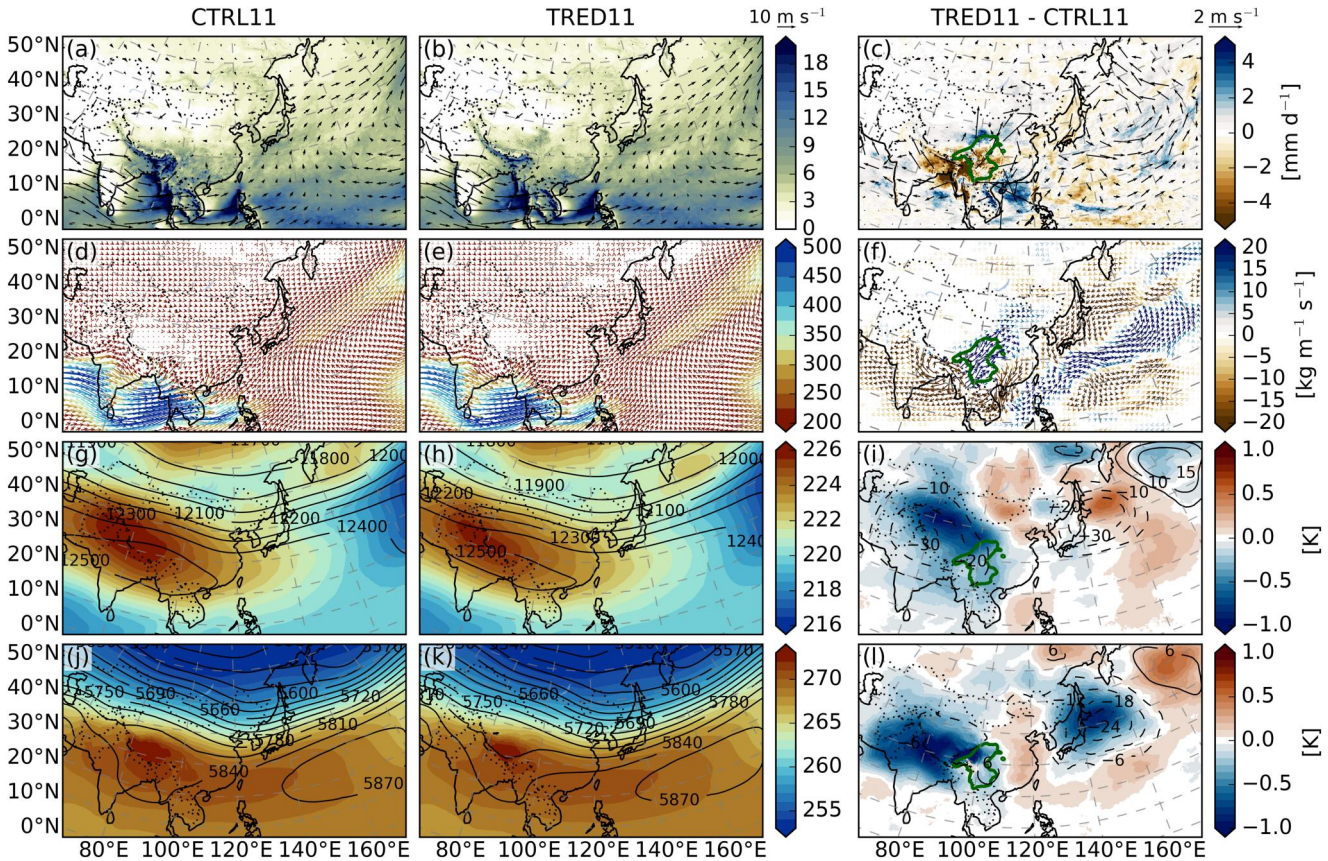


**Figure 7.** Maps of (a–c) Precipitation (contour; units: mm $d^{-1}$) and 850-hPa wind (vector; units: m $s^{-1}$), (d–f) vertically integrated water vapor transport (units; kg $m^{-1}$ $s^{-1}$), (g–i) 200-hPa temperature (shading; units: K) and geopotential height (contour; units: meters) and (j–l) 500-hPa temperature (shading; units: K), geopotential height (contour; units: meters) averaged over the rainy season (MJJAS) from the year 2001–2005. From left to right are the results from CTRL11, TRED11 and their differences, respectively. The green line in the difference maps indicates regions with topographic changes greater than 500 m.

## 4. Results

Here we discuss the climate effects of changing the HM geometry (see Figures 1 and 2). In the first two subsections 4.1 and 4.2, we will address the impacts upon the large-scale climate (near and beyond the vicinity of the topographic modifications), and the effects upon the onset of the monsoon. As remote effects are much more pronounced when reducing the height of the HM, we will restrict discussion to TRED11 in these sections. In Section 4.3, we will discuss the effects on the regional climate in the vicinity of the HM and will address both TRED and TENV experiments.

### 4.1. Imprints on Large-Scale Climate

Figures 7a–7c display precipitation and low-level wind averaged over the rainy season. In CTRL11, heavy precipitation is located in the northeastern BoB, southeastern SCS and western North Pacific (WNP) (Figure 7a). In TRED11, precipitation intensity over the HM, northern BoB and northern Myanmar decreases compared to CTRL11, while precipitation increases in the northeastern TP and SCS (Figure 7c). The large-scale imprint of the topography change can be found along a southwest-northeast-oriented belt over WNP (Figure 7c). Changes in East Asian precipitation patterns agree well with a study by Yu et al. (2018), in which a similar topographic modification experiment was performed with a regional climate model nested in a global climate model.

Water vapor transport plays a pivotal role in the Asian summer monsoon system (T. Zhou & Yu, 2005). In CTRL11, the Indian monsoon transports vast amounts of moisture from the Arabian Sea and the BoB toward the HM and the Indochina Peninsula (Figure 7d). The onshore flow is compelled to rise upon reaching the coastal region of Myanmar, which is characterized by a narrow plain bordered by a mountain range. As the monsoon

moves inland, it brings significant rainfall to the HM. The Indian monsoon travels across the Indochina Peninsula and the SCS then converges with the Southeast Asian monsoon, which carries moisture from the SCS and the WNP into eastern China (R. Huang et al., 1998; Simmonds et al., 1999; Renhe, 2001; T. Zhou & Yu, 2005). In contrast, the reduction of the HM in TRED11 weakens the large-scale monsoon circulation, leading to decreased eastward water vapor flux transport in the coastal region of Myanmar and upstream of the HM region (Figure 7f). This finding aligns well with Yu et al. (2018), where adding the southeastern TP strengthens the monsoon circulation and increases precipitation over the BoB. The orographically triggered precipitation in the southwestern HM also significantly decreases due to the topographic modification and the overall weaker monsoon circulation. Without the HM serving as a barrier, the warm tropical water vapor from the BoB flows northeastwards into northern China before encountering the Qilian Mountains, resulting in increased precipitation there. Furthermore, there is a reduction in moisture transport from the SCS to southeastern China, leading to increased local precipitation over the SCS region. More distantly, strong convergence of the subtropical and extratropical water vapor flux anomalies is found at approximately 30°N between 140 and 170°E, favoring strengthened precipitation over the WNP (Figure 7f).

The change in water vapor transport is closely tied to the alteration in monsoon circulation, which is in turn influenced by topography (Huber & Goldner, 2012; B. Wang et al., 2008; R. Zhang et al., 2015; Z. Zhang et al., 2004). To scrutinize the circulation changes governing water vapor transport, we examine how thermodynamic structure alters in response to topographic modifications (Figures 7g–7l). In CTRL11 featuring modern topography, the Asian landmass—including the Indian subcontinent—undergoes more rapid heating during the summer months than the surrounding ocean. This leads to the formation of a low-pressure system over the land and a persistent high-pressure system over the ocean (Figure 7j). As observed in previous studies (Boos & Kuang, 2010), the upper-tropospheric temperature displays a maximum located south of the Himalayas. Thermal forcing from continental India and the TP triggers the formation of an anticyclone in the upper troposphere (not shown). Driven by the pressure gradient, the thermal effect of land-sea contrast propels the South Asian summer monsoon circulation. In the lower troposphere, the monsoon's westerlies travel from the Indian Ocean and converge with the southwesterly trades at the low-level North Pacific subtropical anticyclonic ridge, forming the southwesterlies (Figure 7a) (Z. Zhang et al., 2004).

In TRED11, the reduced diabatic heating induces a significant cooling of the upper troposphere over the southern HM (Figure 7i). The reduction in diabatic heating leads to an anticyclonic change at lower levels and a cyclonic change at upper levels. In the upper troposphere, a barotropic cyclone is found over the WNP, originating in the TP and moving along the upper-level westerly jet stream (Figure 7i). At lower levels, the weakened India westerlies give rise to decreased water vapor transport. Additionally, cooling of the lower atmosphere over the SCS suppresses the Walker circulation over the Indian Ocean, resulting in an overall weakening of the monsoon circulation (Figure 7l). Remotely, the atmospheric response propagates northeastward along the monsoon winds and favors the cyclonic change pattern to the east of Japan (Figure 7f). This circulation pattern curtails the water supply along the northwestern flank of the western Pacific subtropical high, causing decreased precipitation over the coastal region of northeastern China, the Korean Peninsula and Japan.

The effects of the envelope topography on precipitation are more localized and less pronounced due to the smaller relative change in mountain volume. The influences of both the envelope and reduced topography on the local HM climate, with particular emphasis on (extreme) precipitation indices, will be discussed in Sect. 4.3.

### 4.2. Effect of Topographic Changes on Monsoon Precipitation Onset

Figure 8 shows the Hovmöller diagrams that illustrate the seasonal precipitation cycle, which is zonally averaged over the BoB, HM and eastern China. The shift from the dry season to the rainy season is vividly depicted in the latitude-time cross-sections of mean precipitation. We first discuss the situation in the CTRL11 climate (left-hand panels in Figure 8). The transition from the dry to rainy season upwind of the HM happens quite suddenly around the latitude of approximately 25°N, typically occurring around mid-March (Figure 8a). Before this transition, the rainfall belt remains relatively stable over the southern BoB, located south of 10°N (Figure 8a). However, after mid-March, there's a noticeable northward shift in the near-equatorial rainfall belt. This belt gradually moves northwards, merging with the HM rainfall belt by mid-May. This gradual migration is in contrast to the abrupt transition observed in Myanmar (Figure 8b). There, a substantial increase in rainfall occurs early in May, which signifies the onset of the monsoon over the Indochina peninsula. This onset process aligns with observations

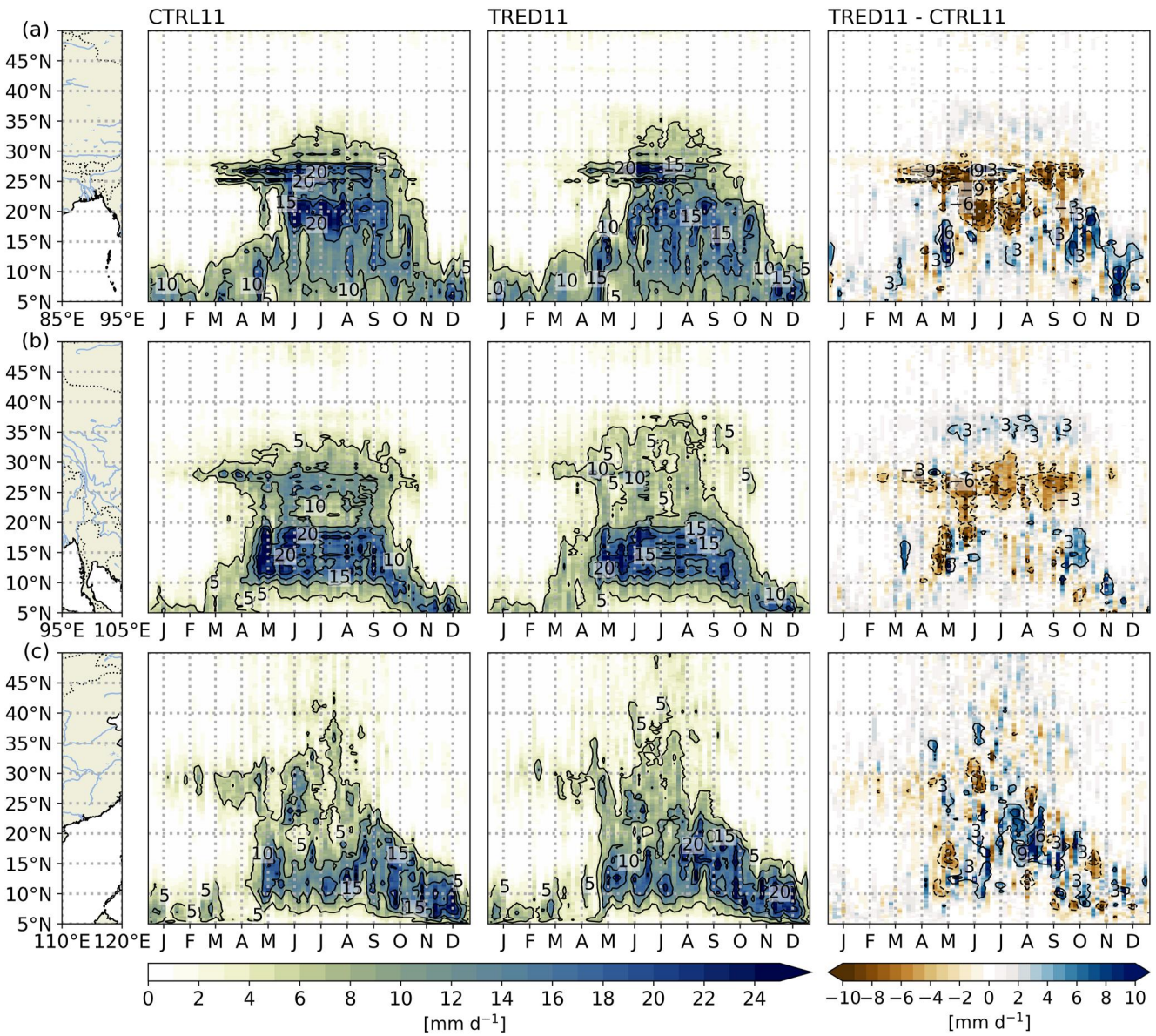


**Figure 8.** Hovmöller diagrams of the seasonal precipitation cycle zonally averaged over (a) Bay of Bengal (85–95°E), (b) Hengduan Mountains (95–105°E) and (c) eastern China (110–120°E) in mm $d^{-1}$. A 5-day moving average has been applied to the 5-year climatology to remove high-frequency variability.

documented in previous studies (Y. Ding & Chan, 2005; B. Wang & LinHo, 2002). Over the SCS, the rainy season typically commences around mid-May, as shown in Figure 8c. This occurrence is a result of the eastward expansion of the southwesterly monsoon into the SCS region, accompanied by the eastward retreat of the western Pacific subtropical high (Z. Zhang et al., 2004).

After reducing the HM's elevation (TRED11, middle panels in Figure 8), both the shift from the dry season to the rainy season and the precipitation intensity experience notable changes. However, the effects vary across different regions. Over Bangladesh and northeasternmost India, the onset of the rainy season is delayed by approximately one month, starting around mid-April. Additionally, precipitation intensity throughout the rainy season typically decreases by approximately 10 mm $d^{-1}$ (Figure 8a). In the northern BoB, while the start of the rainy season remains consistent, there is a noticeable decrease in precipitation intensity. Over the HM, the precipitation intensity during the rainy season also declines, but not as significantly as it does upwind, underscoring the role of the mountains in orographic rainfall (Figure 8b). Over the SCS, we observe an increase in rainfall in July and August, which is consistent with our previous discussion. The mountains affect the surrounding circulation, reducing the

amount of water transported to mainland China, and subsequently increasing local rainfall in the SCS (Figure 8c). Nonetheless, the Hovmöller diagram reveals that the thermal forcing of the HM, which impacts the circulation, begins to exert its influence at a later stage during the advance of the Asian summer monsoon. This observation aligns with previous research by Z. Zhang et al. (2004).

### 4.3. Effects on Regional Climate

The evaluation presented in Section 3.2 reveals that the ET/HM climate, particularly mean rainy season precipitation in terms of patterns and magnitudes, is overall very similar between CTRL11 and CTRL04. However, when considering precipitation indices investigated in this section, CTRL04 generally outperforms CTRL11 (see Figure 6). For these reasons, we have opted to discuss the results of the CPM simulations exclusively in this section. Figure 9 shows the maps of vertically integrated water vapor flux, precipitation indices and convective available potential energy (CAPE) over the HM. Statistics over the HM and its sub-regions are computed over the rainy season and presented in Table 3.

Figure 9a depicts the water vapor transport in the ET region during the rainy season in CTRL04. The atmospheric water flux is approximately parallel to the elevation gradient on the southwestern side of the HM. This causes the distinctive spatial distribution of climatological rainy-season precipitation, which leads to pronounced orographic precipitation in easternmost India and northernmost Myanmar, as shown in Figure 9d. A secondary peak is visible at the western side of the Sichuan Basins (WSSB). The average daily precipitation during the rainy season and simulation period upwind of the HM amounts to 12.7 mm $d^{-1}$. Over the HM, high precipitation amounts often coincide with local topographic peaks, whereas the valleys often receive smaller precipitation amounts due to rain-shadow effects. On average, the daily precipitation over the central HM is 7.2 mm $d^{-1}$. Figures 9g and 9j show the extreme daily precipitation p99D and extreme hourly precipitation p99.9H in CTRL04. For both extreme precipitation indices, maxima are found southwest of the HM, along the Indian/Myanmar border, and over the BoB and its adjacent land area. In the area upwind of the HM, p99D averages to 97.0 mm $d^{-1}$, while p99.9H reaches 29.4 mm $hr^{-1}$. In contrast to mean precipitation, the distinct signature of the eastern HM is not evident, with p99D and p99.9H reaching 56.5 mm $d^{-1}$ and 17.3 mm $hr^{-1}$ in HMC, respectively. Central China experiences more intense extreme precipitation compared to the central and eastern HM. This pattern reflects the distribution of the convective available potential energy (CAPE) and is consistent with the fact that daily/hourly precipitation extremes are more related to convective-triggered precipitation events (i.e., thunderstorms) than to orographically induced or stratiform precipitation (Figure 9m).

In TRED04, the absence of a topographic barrier that alters atmospheric circulation leads to a shift in the direction of water vapor flux to the northeast (Figure 9b). This change results in a 33% decrease in mean precipitation upwind of the HM and an 18% reduction over the central HM. Conversely, precipitation increases in the northern HM (Figure 9e). Figures 9h–9k display the changes in extreme daily precipitation p99D and extreme hourly precipitation p99.9H between CTRL04 and TRED04. Over the HM region, where topographic changes exceed 500 m, the spatial patterns of different precipitation indices exhibit substantial variation. The distribution of changes in extreme daily precipitation displays a distinct pattern (Figure 9h), as the northern part of HM experiences an increase in extreme daily precipitation after elevation reduction, while the rest remains almost unchanged (Figure 9h). On average, the HMC region sees an increase of 8%, while the upwind region experiences a decrease of 12%. Moreover, changes in extreme hourly precipitation contrast with that of mean precipitation, with nearly the entire region with modified topography experiencing an increase in extreme hourly precipitation, averaging to an increase of 20% (Figure 9k). We assume that this more uniform change in hourly extreme precipitation is caused by a combined effect of higher surface temperatures and a deeper atmosphere, which favors convection. This hypothesis is confirmed by the change in simulated CAPE as seen in Figure 9n. Specifically, the increase in CAPE is most prominent in the central and southern HM in TRED04. In addition to changes in precipitation, there is a notable decrease in net water flux at the surface (i.e., runoff) across the entire HM region, amounting to a 40% decrease. This includes a substantial decrease of 51% in runoff upwind of the mountains and a more moderate reduction of 35% over the HMC region.

The summer mean precipitation in TENV04 exhibits two peaks, similar to the CTRL04 simulation, with one located over the western HM and the other over the WSSB (not shown). Figure 9c shows the spatial distribution and magnitude of differences between CTRL04 and TENV04 for integrated water vapor flux. The topographic change in TENV04 results in less moisture transport from the ocean. However, the western HM experiences a

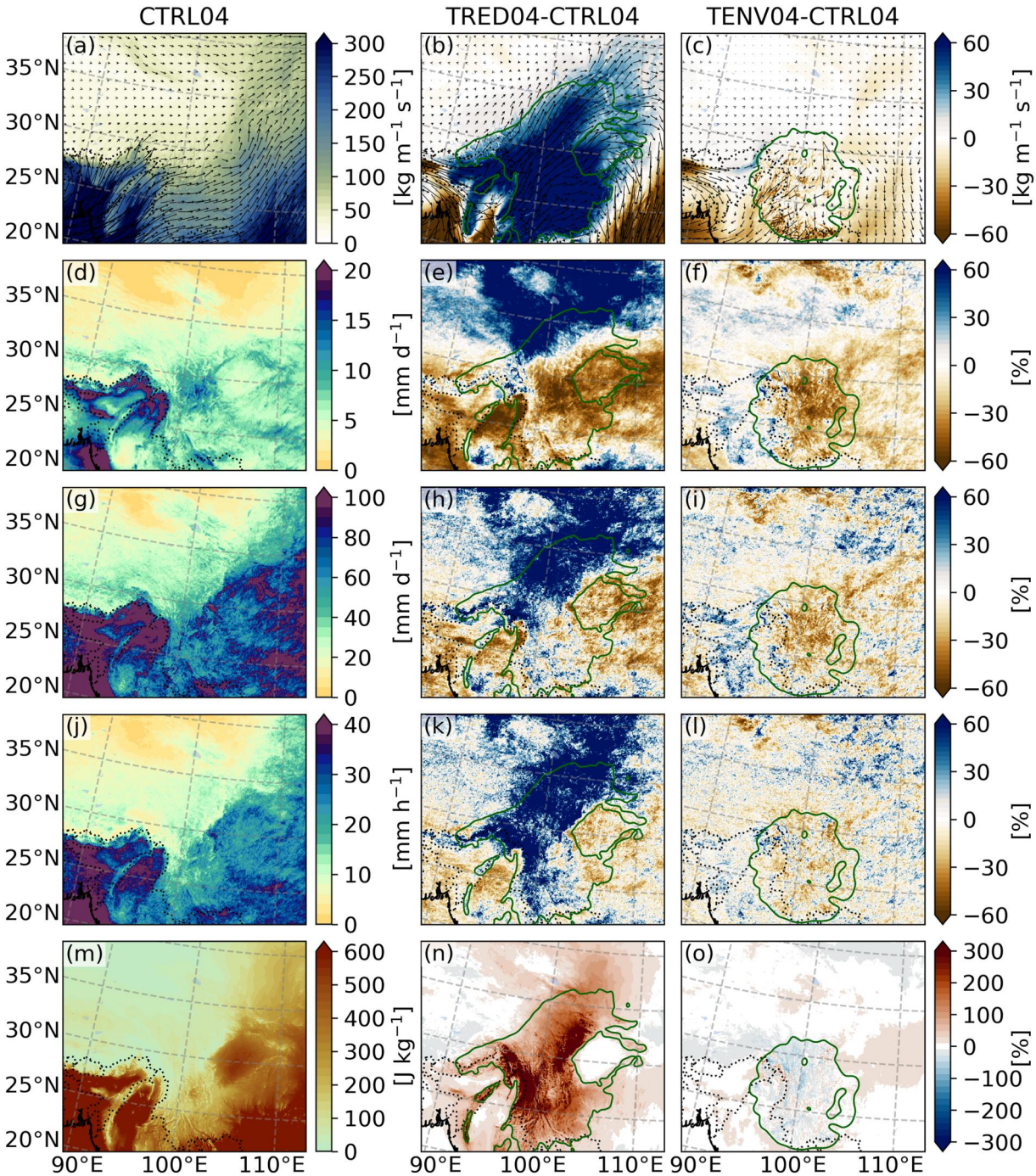


**Figure 9.** (a–c) Vertically integrated water vapor flux, (d–f) mean precipitation, (g–i) the 99th percentile of daily precipitation (p99D), (j–l) the 99th percentile of hourly precipitation (p99.9H) and (m–o) convective available potential energy (CAPE) during the rainy season. From left to right are the results from CTRL04 and the differences between TRED04 and TENV04 with respect to CTRL04. Regions with topographic changes greater than 500 m are delineated by the green line in the differences maps.

very small increase in precipitation (see Figure 9f) probably due to enhanced orographic precipitation caused by the larger mountain volume (Imamovic et al., 2019). A few dry valleys in the north, such as the Three Parallel Rivers (i.e., Salween, Mekong, and Yangtze), experience increased precipitation in the TENV scenario due to the vanished rain shadowing effect. However, in the majority of the central and eastern HM region, mean precipitation during the rainy season decreases substantially (−19%), amounting to a very similar reduction as in TRED.

**Table 3**
*Changes in Precipitation in the Hengduan Mountains and Its Sub-Regions (Figure 1c) for the Topographic Modification Experiments With Reduced Topography (TRED04) and Envelope Topography (TENV04)*

| | HM | | | HMU | | | HMC | | |
|---|---|---|---|---|---|---|---|---|---|
| | CTRL | TRED | TENV | CTRL | TRED | TENV | CTRL | TRED | TENV |
| P [mm $d^{-1}$] | 8.2 | 6.4 (−1.9) | 7.1 (−1.1) | 12.7 | 8.5 (−4.2) | 12.7 (+0.1) | 7.2 | 5.9 (−1.3) | 5.8 (−1.3) |
| P [%] | | −23 | −13 | | −33 | +0 | | −18 | −19 |
| p99D [mm $d^{-1}$] | 64.3 | 65.8 (+1.5) | 58.2 (−6.1) | 97.0 | 85.7 (−11.4) | 95.9 (+1.1) | 56.5 | 61.1 (+4.5) | 49.3 (−7.3) |
| p99D [%] | | +2 | −10 | | −12 | +1 | | +8 | −13 |
| p99.9H [mm $d^{-1}$] | 19.6 | 22.3 (+2.7) | 18.5 (−1.1) | 29.4 | 29.0 (−0.4) | 28.7 (+0.7) | 17.3 | 20.7 (+3.4) | 16.1 (−1.2) |
| p99.9H [%] | | +14 | −6 | | −1 | +2 | | +20 | −7 |
| P − Q [mm $d^{-1}$] | 5.5 | 3.3 (−2.2) | 4.5 (−1.0) | 9.4 | 4.6 (−4.8) | 9.4 (+0.0) | 4.6 | 3.0 (−1.6) | 3.4 (−1.2) |
| P − Q [%] | | −40 | −18 | | −51 | +0 | | −35 | −26 |

*Note*. Statistics are computed over the rainy season (MJJAS) and the years 2001–2005. P refers to mean precipitation, p99D to the daily 99th percentile, p99.9H to the hourly 99.9th percentile and P − Q to precipitation minus evaporation (i.e., the net water flux at the surface).

On the WSSB, the upward motions play a crucial role in the changes in precipitation (Tao et al., 2020). A smoother terrain over the HM in TENV04 leads to a more streamlined atmospheric flow, with less turbulence and mixing, which inhibits the formation of clouds and precipitation. This result is explained through differences in vapor transport and stability between CTRL04 and TENV04 in the following section. Figure 9i shows changes in extreme daily precipitation in TENV04, which largely mirror the spatial pattern of changes in mean precipitation. These changes include an increase in heavy daily precipitation over the western HM and a decrease in the northeastern HM. Figure 9l reveals that the spatially coherent decrease in precipitation indices for the northeastern HM is not apparent for hourly extreme precipitation, which is consistent with the change in CAPE, as shown in Figure 9o. Compared to CTRL04, the simulated CAPE over the HM in TENV04 decreases, although the change is very small compared to changes in TRED04. This is reflected in the modest and less consistent changes observed in extreme hourly precipitation. Notably, the envelope topography resulted in a 26% reduction in surface net water flux over the HMC. This reduction suggests a positive precipitation-erosion feedback for this region, where high-relief topography favors conditions for increased mean precipitation, which accelerates erosion and the further formation of a more pronounced terrain relief.

To further analyze thermodynamic and dynamic processes during the rainy season, we examine how the along-section wind, moisture, vertical velocity, total diabatic heating, and equivalent potential temperature ($\theta_e$) change at different atmospheric heights with modified HM geometries. Figure 10 shows a transect that crosses the HM and is approximately parallel to the prevailing (lower-level) wind direction (see top left of Figures 10a and 1b for location).

By examining the distribution of precipitation depicted in Figure 9a, it is evident that the western boundaries of HM, facing the windward direction, receive a larger proportion of rainfall compared to other orographic features (e.g., WSSB at ∼105°E) located further downwind. The reduction in precipitation observed in areas downwind can be attributed to variations in specific humidity (Figure 10a). The vertical transect of total diabatic heating across the HM reveals two distinct maxima of upward motions (Figure 10d), one at the southern flanks of the Himalayas at ∼92°E and another over the eastern HM, where the significant upward motion can reach up to the 200 hPa pressure level. On the southern flanks of the Himalayas, the surface fluxes from the non-elevated part of northern India play an important role in the large-scale South Asian monsoon by changing the meridional temperature gradient between northern India and the equator (Boos & Kuang, 2013). The precipitation on the WSSB is mainly caused by the vertical moisture flux convergence (Tao et al., 2020) and is related to the vertical distribution of upward motions (Figure 10d). In the southwestern HM, upward motions and diabatic heating are centered near the surface of the windward slopes. This suggests that mechanical lifting due to orographic forcing is a contributing factor. The topography of the HM acts as a barrier to the southwest winds, leading to the generation of lower-level convergence, which contributes to horizontal moisture flux convergence and upward motions.

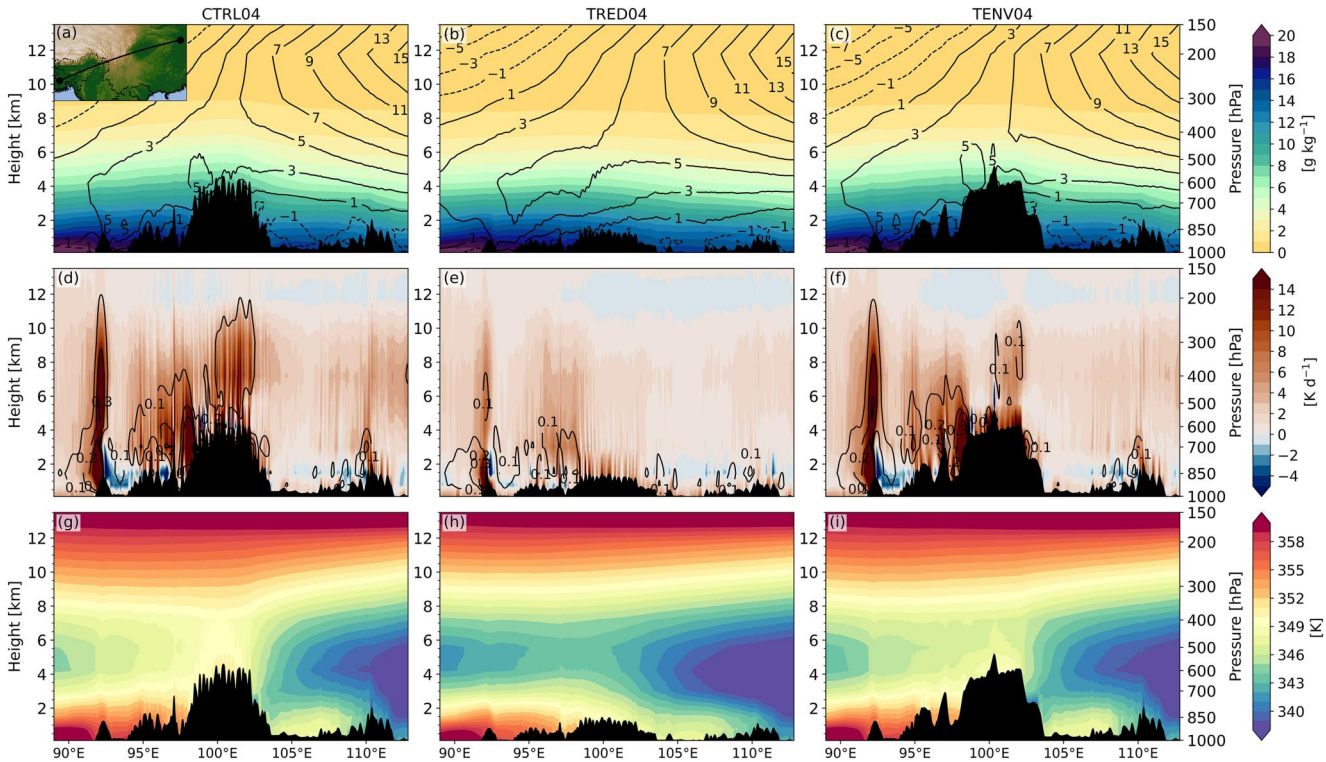


**Figure 10.** Vertical cross sections of (a–c) specific humidity (shading) and along-section horizontal wind (contour; units: m s$^{-1}$), (d–f) total diabatic heating (shaded; units: K d$^{-1}$) and vertical velocity (contour; units: pa s$^{-1}$), and (g–i) equivalent potential temperature ($\theta_e$) averaged over the rainy season (MJJAS). The topography is shaded in black. (left column) Modern topography experiment, (middle column) reduced topography experiment and (right column) envelope topography experiment.

Figure 10b displays the moisture availability and along-section wind in the reduced topography experiment, which reveals an intensification of south-westerly winds and a decrease in moisture supply compared to CTRL04. Comparing the diabatic heating over the HM between CTRL04 and TRED04 (Figures 10d and 10e), it is apparent that the reduction of the mountain range significantly weakens the diabatic heating and the upward movement over the mountains, especially over the eastern HM where the moisture flux convergence is an important factor for local precipitation. Moreover, the reduction of the mountain range has a significant impact on diabatic heating to the west of the mountain range at ~92°E (Figure 10e). Additionally, the vertical transects of $\theta_e$ across the HM (Figures 10g and 10h) reveal decreased values in TRED04 at intermediate heights relative to CTRL04, indicating a less stable atmosphere in TRED04, favoring higher convective activities (i.e., heavy hourly precipitation). These findings suggest that the HM affect the Asian monsoon through both orographic insulation and plateau heating.

The general patterns of moisture and along-section winds are very similar in CTRL04 and TENV04 (Figures 10a and 10c). However, differences in the strength of winds and the availability of moisture do exist. In TENV04, southwesterly winds are stronger over the mountains, which contributes to the intensified precipitation on the windward slopes (Figure 9f). The presence of filled valleys in TENV04 leads to an overall increase in surface elevation, which results in a reduction of near-surface specific humidity over the HM. This reduction can be attributed to lower temperatures and saturation vapor pressure at higher elevations. Apart from the direct changes in elevation, the filled valleys also create a more effective barrier to moisture flow, increasing the depletion of water vapour due to orographic precipitation. This, in turn, limits the amount of moisture that can be transported further into the interior of the region. Figure 10f shows the vertical transect of vertical velocity and total diabatic heating in TENV04. Comparing these results with CTRL04 reveals a reduction in diabatic heating and upward movement over the eastern HM. Inspection of $\theta_e$ shows decreased near-surface values in TENV04 relative to CTRL04 (Figure 10i). The modified topography obstructs the transport of moisture to the eastern HM and the WSSB, resulting in a more stable atmosphere.

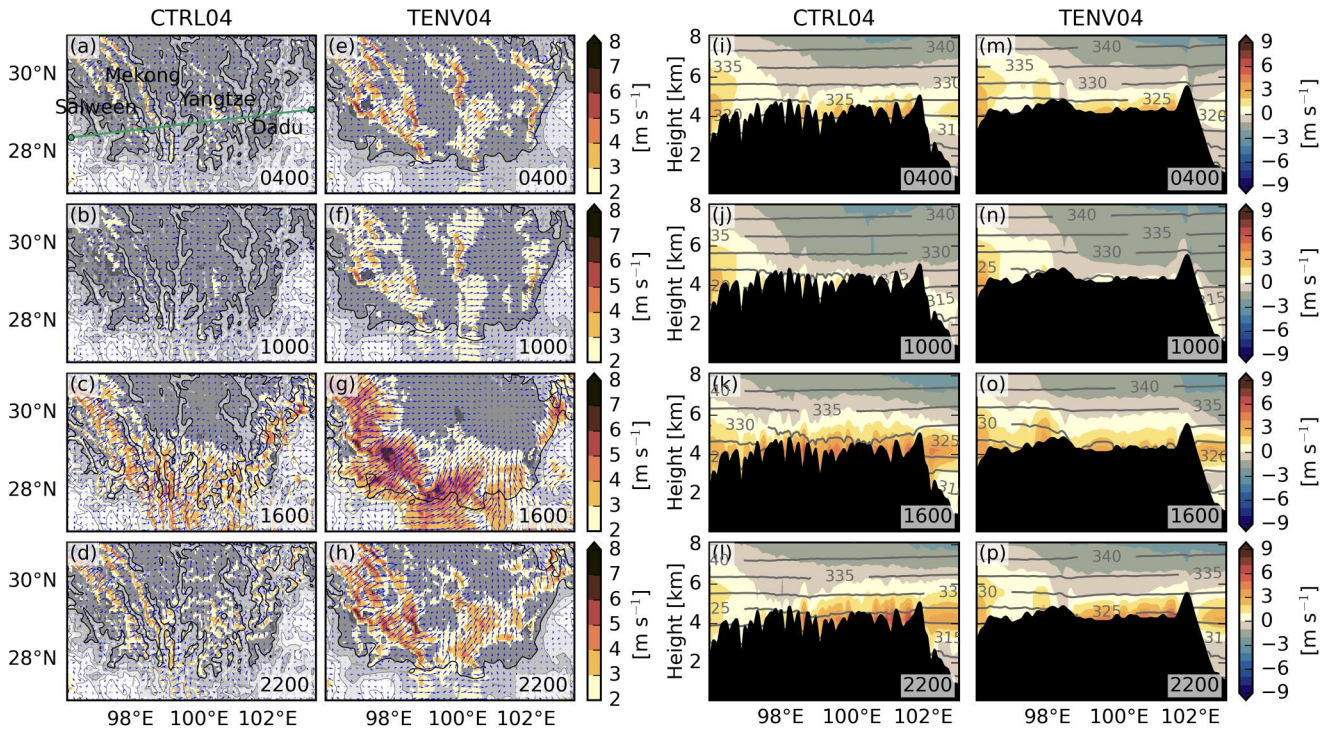


**Figure 11.** Mean diurnal cycle of the surface winds during the rainy season (MJJAS). Left-hand panels show the wind speed (shading) and direction (vectors) at 10 m above ground for CTRL04 (a–d) and TENV04 (e–h). Gray shading indicates the terrain height (1,000 m contour interval) and the bold black line indicates the 4,000 m contour. Right-hand panels show a vertical cross-section through the Three Parallel Rivers (see green line in panel (a)) for CTRL04 (i–l) and TENV04 (m–p). It depicts the wind component normal to the cross-section (shading; positive for northerly flow and negative for southerly flow) and potential temperature (gray contours; units: K). Local time is indicated in the bottom right corner.

To complement the more localized perspective of the envelope experiment, the diurnal cycle of valley winds across the Three Parallel Rivers, averaged over the rainy season, is shown in Figure 11 for both the CTRL04 and TENV04 scenarios. At the end of the night (04:00), CTRL04 simulates an almost quiescent atmosphere at the surface of the river valleys (Figure 11a). By late morning (10:00), the up-valley flow begins to develop, becoming more pronounced in the southern Mekong and Yangtze river valleys (Figure 11b). In the late afternoon (16:00), the up-valley wind intensifies in the Yangtze and Dadu river valleys, predominantly flowing in a south-north direction. However, in the Salween and Mekong valleys, the up-valley wind is noticeable only in the southern part of the domain, while in the north, southeastern winds prevail (Figure 11k). Finally, during the evening (22:00), the Yangtze and Dadu exhibit a light up-valley flow (Figure 11l). In the Salween and Mekong, the flow is dominated by weaker southeasterlies compared to those in the afternoon (Figure 11d). Compared to CTRL04, TENV04 exhibits much stronger surface winds throughout the day, attributed to decreased surface roughness (Figures 11e–11h). However, the along-valley surface wind component, perpendicular to the cross-section, is significantly weaker than in CTRL04 (Figure 11o). This difference is particularly evident in the eastern region of the HM, where the predominant surface wind runs from south to north. This configuration leads to a more stable atmosphere, consequently resulting in a reduction in precipitation over the HM.

## 5. Discussion and Conclusions

In this study, we applied the limited-area model COSMO with a large-scale simulation at a horizontal resolution of 12 km, covering an extended CORDEX East Asia domain, and a nested convection-permitting simulation at a horizontal resolution of 4.4 km, covering the Hengduan Mountains (HM), including parts of southwestern China and Indochina. We first evaluated the model's ability to simulate the control climate for the period 2001–2005 (CTRL). We then proceeded with two sensitivity experiments involving modified HM topography scenarios—a first scenario with a spatially heterogeneous reduction of the HM (TRED) and a second scenario with an envelope topography, in which the deep valleys were filled (TENV). To our knowledge, this is the first terrain modification experiment conducted over the Tibetan Plateau (TP) using a convection-permitting model (CPM).

The improved representation of precipitation frequency and intensity in CPMs allowed us to study the sensitivity of these processes on the mountain geometry. This approach also allowed us to investigate the complex interplay of HM topography, large-scale processes and localized convective systems. The main findings of these experiments are summarized below, followed by a section, in which we embed the results in a broader context, and an outlook.

1. Validation results demonstrate the ability of the control simulations (using 12 and 4.4 km grid spacings) to simulate the climate over East Asia and the HM region for the period 2001–2005. The simulated precipitation reproduces the spatial variations well, albeit with a slight underestimation over India and the South China Sea (SCS). Moreover, our simulation features lower precipitation biases over the TP compared to previous modeling efforts owing to a higher spatial resolution (B. Huang et al., 2015; D. Wang et al., 2013; W. Zhou et al., 2016). The simulated monsoon reproduces the temporal and latitudinal progression of both the Indian and East Asian monsoon precipitation. Over the HM, both CTRL11 and CTRL04 capture the seasonal precipitation cycle well, but reveal an onset of the summer monsoon that is seasonally too early. An additional validation against in situ rain gauge station data reveals that the explicit representation of convection at finer spatial resolution is beneficial for reproducing accurate magnitudes of wet day frequencies and the spatial range of precipitation intensities on a daily/hourly scale.
2. TRED results show that the HM acts as a topographic barrier, resulting in pronounced orographic precipitation in easternmost India and northernmost Myanmar. The study also reveals an increase in diabatic heating over the uplifted HM, which triggers circulation changes around the uplifted region and strengthens the westerly wind from the ocean in South Asia. Consequently, there is a marked intensification of precipitation in Indochina and southwestern China, along with decreased precipitation in the SCS. Additionally, the strengthened cyclonic circulation in the Bay of Bengal extends eastward, indicating an intensification of the East Asian summer monsoon upon the uplift of the HM. However, the uplift of the HM causes a shallower and more stable atmosphere locally, leading to less convective activity and thus decreased extreme hourly precipitation.
3. In contrast to TRED, the TENV's remote effects on climate are negligible. TENV results indicate that the removal of valleys is associated with an overall reduction in precipitation and runoff. In the HM upstream region, spatially integrated precipitation slightly increases, but the central and eastern HM experience a marked drying. This finding suggests a positive feedback mechanism between precipitation and erosion—at least for this region with its specific terrain configuration and flow regime during monsoon.

Geological evidence shows that the southern two-thirds of the HM have grown higher in the latest Miocene or Pliocene (Hoke et al., 2014). Additionally, geological studies indicate that northeastern India experienced a more humid climate between the Late Miocene to Pliocene (Hoorn et al., 2000). Thus, both the geological evidence and the simulations conducted in this study support the notion that the uplift of the HM contributes to the intensification of the Asian monsoon. However, some relations remain uncertain. Molnar and Rajagopalan (2012) linked the more arid northwestern Indian subcontinent between 11 and 7 million years ago to the growth of the eastern margin of the TP. While in our study, the reduction in topography does not result in a significant change in precipitation in northwestern India. Therefore, if the uplift of the eastern TP is not the primary cause, the arid climate in northwestern India may be more closely related to the global climatic cooling (H. Lu & Guo, 2014).

The HM's complex interaction with monsoon systems has created a complex regional and local climate, where dissected topography from erosion further enhances precipitation. This unique feedback between topography and climate has likely shaped the complex topographic and climatic heterogeneity of the region, providing a wide diversity of habitats for species (Antonelli et al., 2018). Therefore the unique combination of tectonic uplift and the monsoon system has created unique conditions for biodiversity (W.-N. Ding et al., 2020).

Further studies are needed to assess the influence of different HM geometries on both regional and large-scale climates under different climate conditions. Specifically, it would be intriguing to explore whether the observed climate response to reduced HM topography is consistent across different paleoclimates, such as the Last Glacial Maximum with globally colder temperatures or periods of warmer temperatures. Another compelling area for investigation involves examining if imprints of topography on large-scale circulation depend on atmospheric oscillations or modes, such as the El Niño-Southern Oscillation and Indian Ocean Dipole, which are both thought to influence the interannual variability of the Asian summer monsoon (Pothapakula et al., 2020). Addressing this question would necessitate longer simulation periods; however, the substantial computational

costs of fine-scale, convection-permitting simulations currently pose a significant challenge. With a resolution of 4.4 km, we are able to resolve the main valleys of the HM (see Figure 2a)—however, local wind systems that could influence precipitation are still not fully resolved. Running simulations with even finer grid spacings would therefore shed more light on the complex influence of (small-scale) terrain relief on precipitation formation. Regarding the envelope topography experiment, we noted that lower-level atmospheric flow is predominantly perpendicular to the main valleys and obtained results might therefore be limited to this specific configuration. Additional experiments with more valley-aligned flow would thus nicely complement the findings of this study.

## Data Availability Statement

The ERA5 reanalysis data are available at the Copernicus Climate Change Service (C3S) Climate Data Store via https://doi.org/10.24381/cds.bd0915c6 (Hersbach et al., 2018). The APHRODITE precipitation data are available at http://aphrodite.st.hirosaki-u.ac.jp/download (APHRODITE V1101EX, 2018). The AphroTemp temperature data are available at http://aphrodite.st.hirosaki-u.ac.jp/download (AphroTemp V1808, 2018). The CRU temperature data are available at https://www.metoffice.gov.uk/hadobs/crutem4 (CRUTEM4, 2012). The GPM IMERG precipitation data are available at https://disc.gsfc.nasa.gov via https://doi.org/10.5067/GPM/IMERGDF/DAY/06 (GPM IMERG, 2020). The GPCC precipitation data are available at https://opendata.dwd.de/climate_environment/GPCC/html/download_gate.html via https://doi.org/10.5676/DWD_GPCC/FD_M_V2022_025 (GPCC, 2022). The PBCOR precipitation data are available at https://www.gloh2o.org/pbcor (PBCOR, 2020). The CMA precipitation data are available at http://data.cma.cn (CMA, 2022). The source code for topography modification is licensed under MIT and published on GitHub: https://github.com/ruolanxixi/HM_Geometries (ruolanxixi, 2024). The weather and climate model COSMO is free of charge for research applications (for more details see: http://www.cosmo-model.org (COSMO, 2022)). The raw model output is too large to provide in an online repository. A post-processed set of the model output as well as the COSMO namelists can be obtained from the corresponding author.

**Acknowledgments**
This research is funded by the ETH+ grant "Biodiversity, Earth, Climate Coupling in Yunnan (Western China)" from ETH Zurich. We acknowledge PRACE for awarding us computational resources at Piz Daint at the Swiss National Supercomputing Center (CSCS). Open access funding provided by Eidgenossische Technische Hochschule Zurich.

## References

Acosta, R. P., & Huber, M. (2020). Competing topographic mechanisms for the summer Indo-Asian monsoon. *Geophysical Research Letters*, *47*(3), e2019GL085112. https://doi.org/10.1029/2019GL085112

Antonelli, A., Kissling, W. D., Flantua, S. G. A., Bermúdez, M. A., Mulch, A., Muellner-Riehl, A. N., et al. (2018). Geological and climatic influences on mountain biodiversity. *Nature Geoscience*, *11*(10), 718–725. https://doi.org/10.1038/s41561-018-0236-z

APHRODITE V1101EX. (2018). APHRO_MA V1101EX_R1 monsoon Asia daily precipitation [Dataset]. *APHRODITE*. Retrieved from http://aphrodite.st.hirosaki-u.ac.jp/download

AphroTemp V1808. (2018). APHRO_MA V1808 temperature [Dataset]. *APHRODITE*. Retrieved from http://aphrodite.st.hirosaki-u.ac.jp/download

Arino, O., Ramos Perez, J. J., Kalogirou, V., Bontemps, S., Defourny, P., & Van Bogaert, E. (2012). Global land cover map for 2009 (GlobCover 2009) [Dataset]. *PANGAEA*. https://doi.org/10.1594/PANGAEA.787668

Asensio, H., Messmer, M., Lüthi, D., Osterried, K., & Jucker, J. (2021). External parameters for numerical weather prediction and climate application EXTPAR v5_6: User and implementation guide [Software]. Retrieved from https://www.cosmo-model.org/content/tasks/workGroups/wg3b/docs/EXTPAR_user_and_implementation_manual_20210906.pdf

Ban, N., Caillaud, C., Coppola, E., Pichelli, E., Sobolowski, S., Adinolfi, M., et al. (2021). The first multi-model ensemble of regional climate simulations at kilometer-scale resolution, part I: Evaluation of precipitation. *Climate Dynamics*, *57*(1–2), 275–302. https://doi.org/10.1007/s00382-021-05708-w

Ban, N., Schmidli, J., & Schär, C. (2015). Heavy precipitation in a changing climate: Does short-term summer precipitation increase faster? *Geophysical Research Letters*, *42*(4), 1165–1172. https://doi.org/10.1002/2014GL062588

Beck, H. E., Wood, E. F., McVicar, T. R., Zambrano-Bigiarini, M., Alvarez-Garreton, C., Baez-Villanueva, O. M., et al. (2020). Bias correction of global high-resolution precipitation climatologies using streamflow observations from 9372 catchments. *Journal of Climate*, *33*(4), 1299–1315. https://doi.org/10.1175/JCLI-D-19-0332.1

Boos, W. R., & Kuang, Z. (2010). Dominant control of the South Asian monsoon by orographic insulation versus plateau heating. *Nature*, *463*(7278), 218–222. https://doi.org/10.1038/nature08707

Boos, W. R., & Kuang, Z. (2013). Sensitivity of the South Asian monsoon to elevated and non-elevated heating. *Scientific Reports*, *3*(1), 1192. https://doi.org/10.1038/srep01192

Botsyun, S., Sepulchre, P., Risi, C., & Donnadieu, Y. (2016). Impacts of Tibetan Plateau uplift on atmospheric dynamics and associated precipitation $\delta^{18}O$. *Climate of the Past*, *12*(6), 1401–1420. https://doi.org/10.5194/cp-12-1401-2016

Bucchignani, E., Montesarchio, M., Cattaneo, L., Manzi, M. P., & Mercogliano, P. (2014). Regional climate modeling over China with COSMO-CLM: Performance assessment and climate projections. *Journal of Geophysical Research: Atmospheres*, *119*(21), 12151–12170. https://doi.org/10.1002/2014JD022219

Cha, D., & Lee, D. (2009). Reduction of systematic errors in regional climate simulations of the summer monsoon over East Asia and the western North Pacific by applying the spectral nudging technique. *Journal of Geophysical Research*, *114*(D14), D14108. https://doi.org/10.1029/2008JD011176

Chang, Y., Gelwick, K., Willett, S. D., Shen, X., Albouy, C., Luo, A., et al. (2023). Phytodiversity is associated with habitat heterogeneity from Eurasia to the Hengduan Mountains. *New Phytologist*, *240*(4), 1647–1658. https://doi.org/10.1111/nph.19206

Chen, D., Dai, A., & Hall, A. (2021). The convective-to-total precipitation ratio and the "drizzling" bias in climate models. *Journal of Geophysical Research: Atmospheres*, *126*(16), e2020JD034198. https://doi.org/10.1029/2020JD034198
Chen, G.-S., Liu, Z., & Kutzbach, J. E. (2014). Reexamining the barrier effect of the Tibetan Plateau on the South Asian summer monsoon. *Climate of the Past*, *10*(3), 1269–1275. https://doi.org/10.5194/cp-10-1269-2014
Clark, M., House, M., Royden, L., Whipple, K., Burchfiel, B., Zhang, X., & Tang, W. (2005). Late Cenozoic uplift of southeastern Tibet. *Geology*, *33*(6), 525. https://doi.org/10.1130/G21265.1
CMA. (2022). Daily/hourly timed data from national surface stations in China [Dataset]. *China Meteorological Administration*. Retrieved from http://data.cma.cn
COSMO. (2022). Consortium for small-scale modeling (COSMO) [Software]. *COSMO*. Retrieved from https://www.cosmo-model.org
CRUTEM4. (2012). Climatic Research Unit (CRU) land station temperature database V4.6.0.0 [Dataset]. *Climatic Research Unit*. Retrieved from https://www.metoffice.gov.uk/hadobs/crutem4
Damseaux, A., Fettweis, X., Lambert, M., & Cornet, Y. (2020). Representation of the rain shadow effect in Patagonia using an orographic-derived regional climate model. *International Journal of Climatology*, *40*(3), 1769–1783. https://doi.org/10.1002/joc.6300
Ding, L., Kapp, P., Cai, F., Garzione, C. N., Xiong, Z., Wang, H., & Wang, C. (2022). Timing and mechanisms of Tibetan Plateau uplift. *Nature Reviews Earth & Environment*, *3*(10), 652–667. https://doi.org/10.1038/s43017-022-00318-4
Ding, W.-N., Ree, R. H., Spicer, R. A., & Xing, Y.-W. (2020). Ancient orogenic and monsoon-driven assembly of the world's richest temperate alpine flora. *Science*, *369*(6503), 578–581. https://doi.org/10.1126/science.abb4484
Ding, Y., & Chan, J. C. L. (2005). The East Asian summer monsoon: An overview. *Meteorology and Atmospheric Physics*, *89*(1–4), 117–142. https://doi.org/10.1007/s00703-005-0125-z
Dong, W., Lin, Y., Wright, J. S., Ming, Y., Xie, Y., Wang, B., et al. (2016). Summer rainfall over the southwestern Tibetan Plateau controlled by deep convection over the Indian subcontinent. *Nature Communications*, *7*(1), 10925. https://doi.org/10.1038/ncomms10925
Duan, A., Li, F., Wang, M., & Wu, G. (2011). Persistent weakening trend in the spring sensible heat source over the Tibetan Plateau and its impact on the Asian summer monsoon. *Journal of Climate*, *24*(21), 5671–5682. https://doi.org/10.1175/JCLI-D-11-00052.1
Fuhrer, O., Osuna, C., Lapillonne, X., Gysi, T., Cumming, B., Bianco, M., et al. (2014). Towards a performance portable, architecture agnostic implementation strategy for weather and climate models. *Supercomputing Frontiers and Innovations*, *1*(1). https://doi.org/10.14529/jsfi140103
Gal-Chen, T., & Somerville, R. C. (1975). On the use of a coordinate transformation for the solution of the Navier-Stokes equations. *Journal of Computational Physics*, *17*(2), 209–228. https://doi.org/10.1016/0021-9991(75)90037-6
Gao, Y., Chen, F., & Jiang, Y. (2020). Evaluation of a convection-permitting modeling of precipitation over the Tibetan Plateau and its influences on the simulation of snow-cover fraction. *Journal of Hydrometeorology*, *21*(7), 1531–1548. https://doi.org/10.1175/JHM-D-19-0277.1
Giorgi, F., & Gutowski, W. J. (2015). Regional dynamical downscaling and the CORDEX initiative. *Annual Review of Environment and Resources*, *40*(1), 467–490. https://doi.org/10.1146/annurev-environ-102014-021217
Giorgi, F., & Mearns, L. O. (1999). Introduction to special section: Regional climate modeling revisited. *Journal of Geophysical Research*, *104*(D6), 6335–6352. https://doi.org/10.1029/98JD02072
GPCC. (2022). Global precipitation climatology centre monthly precipitation dataset from 1891-present version 2022 [Dataset]. *Deutscher Wetterdienst*. https://doi.org/10.5676/DWD{_}GPCC/FD{_}M{_}V2022{_}025
GPM IMERG. (2020). GPM IMERG final precipitation L3 1 day 0.1 degree × 0.1 degree V06 (GPM_3IMERGDF) [Dataset]. *NASA Goddard Earth Sciences (GES) Data and Information Services Center (DISC)*. https://doi.org/10.5067/GPM/IMERGDF/DAY/06
Heise, E., Ritter, B., & Schrodin, R. (2006). Operational implementation of the multilayer soil model. Tech. Rep. *Offenbach am Main: Deutscher Wetterdienst*.
Hersbach, H., Bell, B., Berrisford, P., Hirahara, S., Horányi, A., & Muñoz-Sabater, J. (2018). ERA5 hourly data on pressure levels from 1959 to present [Dataset]. *Copernicus*. Retrieved from https://cds.climate.copernicus.eu/cdsapp#!/dataset/reanalysis-era5-pressure-levels?tab=overview
Hersbach, H., Bell, B., Berrisford, P., Hirahara, S., Horányi, A., Muñoz-Sabater, J., et al. (2020). The ERA5 global reanalysis. *Quarterly Journal of the Royal Meteorological Society*, *146*(730), 1999–2049. https://doi.org/10.1002/qj.3803
Hoke, G. D., Liu-Zeng, J., Hren, M. T., Wissink, G. K., & Garzione, C. N. (2014). Stable isotopes reveal high southeast Tibetan Plateau margin since the Paleogene. *Earth and Planetary Science Letters*, *394*, 270–278. https://doi.org/10.1016/j.epsl.2014.03.007
Hoorn, C., Ohja, T., & Quade, J. (2000). Palynological evidence for vegetation development and climatic change in the Sub-Himalayan Zone (Neogene, Central Nepal). *Palaeogeography, Palaeoclimatology, Palaeoecology*, *163*(3–4), 133–161. https://doi.org/10.1016/S0031-0182(00)00149-8
Huang, B., Polanski, S., & Cubasch, U. (2015). Assessment of precipitation climatology in an ensemble of CORDEX-East Asia regional climate simulations. *Climate Research*, *64*(2), 141–158. https://doi.org/10.3354/cr01302
Huang, R., Zhang, Z., Huang, G., & Ren, B. (1998). Characteristics of the water vapor transport in East Asian monsoon region and its difference from that in South Asian monsoon region in summer. *Chinese Journal of Atmospheric Sciences*, *22*(4), 460–469. https://doi.org/10.3878/j.issn.1006-9895.1998.04.08
Huber, M., & Goldner, A. (2012). Eocene monsoons. *Journal of Asian Earth Sciences*, *44*, 3–23. https://doi.org/10.1016/j.jseaes.2011.09.014
Huffman, G. J., Bolvin, D. T., Braithwaite, D., Hsu, K., Joyce, R., Kidd, C., et al. (2015). NASA global precipitation measurement (GPM) integrated multi-satellite retrievals for GPM (IMERG) [Dataset]. *NASA*. Retrieved from https://gpm.nasa.gov/sites/default/files/2020-05/IMERG_ATBD_V06.3.pdf
Jha, S., Harry, D. L., & Schutt, D. L. (2017). Toolbox for analysis of flexural isostasy (TAFI)—A MATLAB toolbox for modeling flexural deformation of the lithosphere. *Geosphere*, *13*(5), 1555–1565. https://doi.org/10.1130/GES01421.1
Jiang, D., Ding, Z., Drange, H., & Gao, Y. (2008). Sensitivity of East Asian climate to the progressive uplift and expansion of the Tibetan Plateau under the mid-Pliocene boundary conditions. *Advances in Atmospheric Sciences*, *25*(5), 709–722. https://doi.org/10.1007/s00376-008-0709-x
Jiang, Y., Yang, K., Li, X., Zhang, W., Shen, Y., Chen, Y., & Li, X. (2022). Atmospheric simulation-based precipitation datasets outperform satellite-based products in closing basin-wide water budget in the eastern Tibetan Plateau. *International Journal of Climatology*, *42*(14), 7252–7268. https://doi.org/10.1002/joc.7642
Jones, P. D., Lister, D. H., Osborn, T. J., Harpham, C., Salmon, M., & Morice, C. P. (2012). Hemispheric and large-scale land-surface air temperature variations: An extensive revision and an update to 2010. *Journal of Geophysical Research*, *117*(D5), D05127. https://doi.org/10.1029/2011JD017139
Jones, P. W. (1999). First- and second-order conservative remapping schemes for grids in spherical coordinates. *Monthly Weather Review*, *127*(9), 2204–2210. https://doi.org/10.1175/1520-0493(1999)127⟨2204:FASOCR⟩2.0.CO;2
Kaufmann, P. (2008). Association of surface stations to NWP model grid points. In *COSMO newsletter* (pp. 54–55). Retrieved from https://www.cosmo-model.org/content/model/documentation/newsLetters/newsLetter09/cnl9-10.pdf

Kirschbaum, D. B., Huffman, G. J., Adler, R. F., Braun, S., Garrett, K., Jones, E., et al. (2017). NASA's remotely sensed precipitation: A reservoir for applications users. *Bulletin of the American Meteorological Society*, *98*(6), 1169–1184. https://doi.org/10.1175/BAMS-D-15-00296.1

Koseki, S., Watanabe, M., & Kimoto, M. (2008). Role of the midlatitude air-sea interaction in orographically forced climate. *Journal of the Meteorological Society of Japan. Ser. II*, *86*(2), 335–351. https://doi.org/10.2151/jmsj.86.335

Kotlarski, S., Keuler, K., Christensen, O. B., Colette, A., Déqué, M., Gobiet, A., et al. (2014). Regional climate modeling on European scales: A joint standard evaluation of the EURO-CORDEX RCM ensemble. *Geoscientific Model Development*, *7*(4), 1297–1333. https://doi.org/10.5194/gmd-7-1297-2014

Lee, D., Park, C., Kim, Y.-H., & Min, S.-K. (2016). Evaluation of the COSMO-CLM for East Asia climate simulations: Sensitivity to spectral nudging. *Journal of Climate Research*, *11*(1), 69–85. https://doi.org/10.14383/cri.2016.11.1.69

Lee, D.-K., & Cha, D.-H. (2020). Regional climate modeling for Asia. *Geoscience Letters*, *7*(1), 13. https://doi.org/10.1186/s40562-020-00162-8

Leutwyler, D., Fuhrer, O., Lapillonne, X., Lüthi, D., & Schär, C. (2016). Towards European-scale convection-resolving climate simulations with GPUs: A study with COSMO 4.19. *Geoscientific Model Development*, *9*(9), 3393–3412. https://doi.org/10.5194/gmd-9-3393-2016

Li, L., & Zhu, B. (1990). The modified envelope orography and the air flow over and around mountains. *Advances in Atmospheric Sciences*, *7*(3), 249–260. https://doi.org/10.1007/BF03179759

Li, P., Furtado, K., Zhou, T., Chen, H., & Li, J. (2021). Convection-permitting modelling improves simulated precipitation over the central and eastern Tibetan Plateau. *Quarterly Journal of the Royal Meteorological Society*, *147*(734), 341–362. https://doi.org/10.1002/qj.3921

Li, S., Sørland, S. L., Wild, M., & Schär, C. (2023). Aerosol sensitivity simulations over East Asia in a convection-permitting climate model. *Climate Dynamics*, *61*(1–2), 861–881. https://doi.org/10.1007/s00382-022-06620-7

Li, Z., He, Y., Wang, C., Wang, X., Xin, H., Zhang, W., & Cao, W. (2011). Spatial and temporal trends of temperature and precipitation during 1960–2008 at the Hengduan Mountains, China. *Quaternary International*, *236*(1–2), 127–142. https://doi.org/10.1016/j.quaint.2010.05.017

Lin, C., Chen, D., Yang, K., & Ou, T. (2018). Impact of model resolution on simulating the water vapor transport through the central Himalayas: Implication for models' wet bias over the Tibetan Plateau. *Climate Dynamics*, *51*(9–10), 3195–3207. https://doi.org/10.1007/s00382-018-4074-x

Liu, K., Song, C., Ke, L., Jiang, L., Pan, Y., & Ma, R. (2019). Global open-access DEM performances in Earth's most rugged region high mountain Asia: A multi-level assessment. *Geomorphology*, *338*, 16–26. https://doi.org/10.1016/j.geomorph.2019.04.012

Liu, X., & Yin, Z.-Y. (2002). Sensitivity of East Asian monsoon climate to the uplift of the Tibetan Plateau. *Palaeogeography, Palaeoclimatology, Palaeoecology*, *183*(3–4), 223–245. https://doi.org/10.1016/S0031-0182(01)00488-6

Liu, Y., Lu, M., Yang, H., Duan, A., He, B., Yang, S., & Wu, G. (2020). Land–atmosphere–ocean coupling associated with the Tibetan Plateau and its climate impacts. *National Science Review*, *7*(3), 534–552. https://doi.org/10.1093/nsr/nwaa011

Liu, Z., Gao, Y., & Zhang, G. (2022). How well can a convection-permitting-modelling improve the simulation of summer precipitation diurnal cycle over the Tibetan Plateau? *Climate Dynamics*, *58*(11–12), 3121–3138. https://doi.org/10.1007/s00382-021-06090-3

Lu, H., & Guo, Z. (2014). Evolution of the monsoon and dry climate in East Asia during late Cenozoic: A review. *Science China Earth Sciences*, *57*(1), 70–79. https://doi.org/10.1007/s11430-013-4790-3

Lu, M., Yang, S., Zhu, C., Wang, J., Lin, S., Wei, W., & Fan, H. (2023). Thermal impact of the southern Tibetan Plateau on the southeast Asian summer monsoon and modulation by the tropical Atlantic SST. *Journal of Climate*, *36*(5), 1319–1330. https://doi.org/10.1175/JCLI-D-22-0493.1

Ma, Y., Hu, Z., Xie, Q., Meng, X., Zhao, L., & Dong, W. (2022). Convection-permitting modeling over the Tibetan Plateau improves the simulation of Meiyu rainfall during the 2011 Yangtze Plain flood. *Atmospheric Research*, *265*, 105907. https://doi.org/10.1016/j.atmosres.2021.105907

Manabe, S., & Terpstra, T. B. (1974). The effects of mountains on the general circulation of the atmosphere as identified by numerical experiments. *Journal of the Atmospheric Sciences*, *31*(1), 3–42. https://doi.org/10.1175/1520-0469(1974)031⟨0003:TEOMOT⟩2.0.CO;2

Matsumoto, J. (1997). Seasonal transition of summer rainy season over Indochina and adjacent monsoon region. *Advances in Atmospheric Sciences*, *14*(2), 231–245. https://doi.org/10.1007/s00376-997-0022-0

Meng, X., Lyu, S., Zhang, T., Zhao, L., Li, Z., Han, B., et al. (2018). Simulated cold bias being improved by using MODIS time-varying albedo in the Tibetan Plateau in WRF model. *Environmental Research Letters*, *13*(4), 044028. https://doi.org/10.1088/1748-9326/aab44a

Molnar, P., Boos, W. R., & Battisti, D. S. (2010). Orographic controls on climate and paleoclimate of Asia: Thermal and mechanical roles for the Tibetan Plateau. *Annual Review of Earth and Planetary Sciences*, *38*(1), 77–102. https://doi.org/10.1146/annurev-earth-040809-152456

Molnar, P., & Rajagopalan, B. (2012). Late Miocene upward and outward growth of eastern Tibet and decreasing monsoon rainfall over the northwestern Indian subcontinent since ∼10 Ma. *Geophysical Research Letters*, *39*(9), L09702. https://doi.org/10.1029/2012GL051305

Mutke, J., & Barthlott, W. (2005). Patterns of vascular plant diversity at continental to global scale. *Biologiske Skrifter*, *55*, 521–537.

Nearing, M., Jetten, V., Baffaut, C., Cerdan, O., Couturier, A., Hernandez, M., et al. (2005). Modeling response of soil erosion and runoff to changes in precipitation and cover. *Catena*, *61*(2–3), 131–154. https://doi.org/10.1016/j.catena.2005.03.007

Ning, B., Yang, X., & Chang, L. (2012). Changes of temperature and precipitation extremes in Hengduan mountains, Qinghai-Tibet Plateau in 1961–2008. *Chinese Geographical Science*, *22*(4), 422–436. https://doi.org/10.1007/s11769-012-0549-6

Orsolini, Y., Wegmann, M., Dutra, E., Liu, B., Balsamo, G., Yang, K., et al. (2019). Evaluation of snow depth and snow cover over the Tibetan Plateau in global reanalyses using in situ and satellite remote sensing observations. *The Cryosphere*, *13*(8), 2221–2239. https://doi.org/10.5194/tc-13-2221-2019

Paeth, H., Steger, C., Li, J., Pollinger, F., Mutz, S. G., & Ehlers, T. A. (2019). Comparison of climate change from Cenozoic surface uplift and glacial-interglacial episodes in the Himalaya-Tibet region: Insights from a regional climate model and proxy data. *Global and Planetary Change*, *177*, 10–26. https://doi.org/10.1016/j.gloplacha.2019.03.005

Park, H.-S., Chiang, J. C. H., & Bordoni, S. (2012). The mechanical impact of the Tibetan Plateau on the seasonal evolution of the South Asian monsoon. *Journal of Climate*, *25*(7), 2394–2407. https://doi.org/10.1175/JCLI-D-11-00281.1

PBCOR. (2020). Precipitation Bias CORrection [Dataset]. *GloH2O*. Retrieved from https://www.gloh2o.org/pbcor

Pothapakula, P. K., Primo, C., Sørland, S., & Ahrens, B. (2020). The synergistic impact of ENSO and IOD on Indian summer monsoon rainfall in observations and climate simulations – An information theory perspective. *Earth System Dynamics*, *11*(4), 903–923. https://doi.org/10.5194/esd-11-903-2020

Prein, A. F., Ban, N., Ou, T., Tang, J., Sakaguchi, K., Collier, E., et al. (2022). Towards ensemble-based kilometer-scale climate simulations over the third pole region. *Climate Dynamics*, *1*(11–12), 1–27. https://doi.org/10.1007/S00382-022-06543-3

Prein, A. F., & Gobiet, A. (2017). Impacts of uncertainties in European gridded precipitation observations on regional climate analysis. *International Journal of Climatology*, *37*(1), 305–327. https://doi.org/10.1002/joc.4706

Prein, A. F., Gobiet, A., Truhetz, H., Keuler, K., Goergen, K., Teichmann, C., et al. (2016). Precipitation in the EURO-CORDEX 0.11 and 0.44 simulations: High resolution, high benefits? *Climate Dynamics*, *46*(1–2), 383–412. https://doi.org/10.1007/s00382-015-2589-y

Qi, W., Feng, L., Kuang, X., Zheng, C., Liu, J., Chen, D., et al. (2022). Divergent and changing importance of glaciers and snow as natural water reservoirs in the eastern and southern Tibetan Plateau. *Journal of Geophysical Research: Atmospheres*, *127*(7), e2021JD035888. https://doi.org/10.1029/2021JD035888

Raschendorfer, M. (2001). The new turbulence parameterization of LM. In *COSMO newsletter* (pp. 89–97). Retrieved from http://www.cosmo-model.org/content/model/documentation/newsLetters/newsLetter01/newsLetter_01.pdf

Rasmussen, R., Baker, B., Kochendorfer, J., Meyers, T., Landolt, S., Fischer, A. P., et al. (2012). How well are we measuring snow: The NOAA/FAA/NCAR winter precipitation test bed. *Bulletin of the American Meteorological Society*, *93*(6), 811–829. https://doi.org/10.1175/BAMS-D-11-00052.1

Reinhardt, T., & Seifert, A. (2006). A three-category ice scheme for LMK. In *COSMO newsletter* (pp. 115–120). Retrieved from http://www.cosmo-model.org/content/model/documentation/newsLetters/newsLetter06/cnl6_reinhardt.pdf

Renhe, Z. (2001). Relations of water vapor transport from Indian Monsoon with that over East Asia and the summer rainfall in China. *Advances in Atmospheric Sciences*, *18*(5), 1005–1017. https://doi.org/10.1007/BF03403519

Ritter, B., & Geleyn, J.-F. (1992). A comprehensive radiation scheme for numerical weather prediction models with potential applications in climate simulations. *Monthly Weather Review*, *120*(2), 303–325. https://doi.org/10.1175/1520-0493(1992)120⟨0303:ACRSFN⟩2.0.CO;2

Rockel, B., Will, A., & Hense, A. (2008). The regional climate model COSMO-CLM (CCLM). *Meteorologische Zeitschrift*, *17*(4), 347–348. https://doi.org/10.1127/0941-2948/2008/0309

Royden, L. H., Burchfiel, B. C., & van der Hilst, R. D. (2008). The geological evolution of the Tibetan Plateau. *Science*, *321*(5892), 1054–1058. https://doi.org/10.1126/science.1155371

ruolanxixi. (2024). HM_Geometries [Software]. *Zenodo*. https://doi.org/10.5281/zenodo.10622999

Schär, C., Ban, N., Fischer, E. M., Rajczak, J., Schmidli, J., Frei, C., et al. (2016). Percentile indices for assessing changes in heavy precipitation events. *Climatic Change*, *137*(1–2), 201–216. https://doi.org/10.1007/s10584-016-1669-2

Schär, C., Fuhrer, O., Arteaga, A., Ban, N., Charpilloz, C., Di Girolamo, S., et al. (2020). Kilometer-scale climate models: Prospects and challenges. *Bulletin of the American Meteorological Society*, *101*(5), E567–E587. https://doi.org/10.1175/BAMS-D-18-0167.1

Schiemann, R., Demory, M.-E., Mizielinski, M. S., Roberts, M. J., Shaffrey, L. C., Strachan, J., & Vidale, P. L. (2014). The sensitivity of the tropical circulation and Maritime Continent precipitation to climate model resolution. *Climate Dynamics*, *42*(9–10), 2455–2468. https://doi.org/10.1007/s00382-013-1997-0

Schlemmer, L., Schär, C., Lüthi, D., & Strebel, L. (2018). A groundwater and runoff formulation for weather and climate models. *Journal of Advances in Modeling Earth Systems*, *10*(8), 1809–1832. https://doi.org/10.1029/2017MS001260

Schneider, U., Becker, A., Finger, P., Meyer-Christoffer, A., Ziese, M., & Rudolf, B. (2014). GPCC's new land surface precipitation climatology based on quality-controlled in situ data and its role in quantifying the global water cycle. *Theoretical and Applied Climatology*, *115*(1–2), 15–40. https://doi.org/10.1007/s00704-013-0860-x

Sevruk, B., Ondrás, M., & Chvíla, B. (2009). The WMO precipitation measurement intercomparisons. *Atmospheric Research*, *92*(3), 376–380. https://doi.org/10.1016/j.atmosres.2009.01.016

Simmonds, I., Bi, D., & Hope, P. (1999). Atmospheric water vapor flux and its association with rainfall over China in summer. *Journal of Climate*, *12*(5), 1353–1367. https://doi.org/10.1175/1520-0442(1999)012⟨1353:AWVFAI⟩2.0.CO;2

Singh, P., & Kumar, N. (1997). Effect of orography on precipitation in the western Himalayan region. *Journal of Hydrology*, *199*(1–2), 183–206. https://doi.org/10.1016/S0022-1694(96)03222-2

Stephens, G. L., L'Ecuyer, T., Forbes, R., Gettelmen, A., Golaz, J., Bodas-Salcedo, A., et al. (2010). Dreary state of precipitation in global models. *Journal of Geophysical Research*, *115*(D24). https://doi.org/10.1029/2010JD014532

Tang, H., Micheels, A., Eronen, J. T., Ahrens, B., & Fortelius, M. (2013). Asynchronous responses of East Asian and Indian summer monsoons to mountain uplift shown by regional climate modelling experiments. *Climate Dynamics*, *40*(5–6), 1531–1549. https://doi.org/10.1007/s00382-012-1603-x

Tang, J., Wang, S., Niu, X., Hui, P., Zong, P., & Wang, X. (2017). Impact of spectral nudging on regional climate simulation over CORDEX East Asia using WRF. *Climate Dynamics*, *48*(7–8), 2339–2357. https://doi.org/10.1007/s00382-016-3208-2

Tao, W., Huang, G., Lau, W. K. M., Dong, D., Wang, P., & Wen, G. (2020). How can CMIP5 AGCMs' resolution influence precipitation in mountain areas: The Hengduan Mountains? *Climate Dynamics*, *54*(1–2), 159–172. https://doi.org/10.1007/s00382-019-04993-w

Tapponnier, P., Zhiqin, X., Roger, F., Meyer, B., Arnaud, N., Wittlinger, G., & Jingsui, Y. (2001). Oblique stepwise rise and growth of the Tibet Plateau. *Science*, *294*(5547), 1671–1677. https://doi.org/10.1126/science.105978

Tian, Y., Kohn, B. P., Hu, S., & Gleadow, A. J. W. (2015). Synchronous fluvial response to surface uplift in the eastern Tibetan Plateau: Implications for crustal dynamics. *Geophysical Research Letters*, *42*(1), 29–35. https://doi.org/10.1002/2014GL062383

Tiedtke, M. (1989). A comprehensive mass flux scheme for cumulus parameterization in large-scale models. *Monthly Weather Review*, *117*(8), 1779–1800. https://doi.org/10.1175/1520-0493(1989)117⟨1779:ACMFSF⟩2.0.CO;2

Trenberth, K. E., & Zhang, Y. (2018). How often does it really rain? *Bulletin of the American Meteorological Society*, *99*(2), 289–298. https://doi.org/10.1175/BAMS-D-17-0107.1

von Storch, H., Langenberg, H., & Feser, F. (2000). A spectral nudging technique for dynamical downscaling purposes. *Monthly Weather Review*, *128*(10), 3664–3673. https://doi.org/10.1175/1520-0493(2000)128⟨3664:ASNTFD⟩2.0.CO;2

Wang, B. (2006). In J. Mason (Ed.), *The Asian monsoon*. Springer Science & Business Media.

Wang, B., Bao, Q., Hoskins, B., Wu, G., & Liu, Y. (2008). Tibetan Plateau warming and precipitation changes in East Asia. *Geophysical Research Letters*, *35*(14), 14702. https://doi.org/10.1029/2008GL034330

Wang, B., & LinHo (2002). Rainy season of the Asian-Pacific summer monsoon. *Journal of Climate*, *15*(4), 386–398. https://doi.org/10.1175/1520-0442(2002)015⟨0386:RSOTAP⟩2.0.CO;2

Wang, D., Menz, C., Simon, T., Simmer, C., & Ohlwein, C. (2013). Regional dynamical downscaling with CCLM over East Asia. *Meteorology and Atmospheric Physics*, *121*(1–2), 39–53. https://doi.org/10.1007/s00703-013-0250-z

Wang, E., Kirby, E., Furlong, K. P., van Soest, M., Xu, G., Shi, X., et al. (2012). Two-phase growth of high topography in eastern Tibet during the Cenozoic. *Nature Geoscience*, *5*(9), 640–645. https://doi.org/10.1038/ngeo1538

Webster, P. J., Magaña, V. O., Palmer, T. N., Shukla, J., Tomas, R. A., Yanai, M., & Yasunari, T. (1998). Monsoons: Processes, predictability, and the prospects for prediction. *Journal of Geophysical Research*, *103*(C7), 14451–14510. https://doi.org/10.1029/97JC02719

Wicker, L. J., & Skamarock, W. C. (2002). Time-splitting methods for elastic models using forward time schemes. *Monthly Weather Review*, *130*(8), 2088–2097. https://doi.org/10.1175/1520-0493(2002)130⟨2088:TSMFEM⟩2.0.CO;2

Wickert, A. D. (2016). Open-source modular solutions for flexural isostasy: gFlex v1.0. *Geoscientific Model Development*, *9*(3), 997–1017. https://doi.org/10.5194/gmd-9-997-2016

Wu, G., He, B., Duan, A., Liu, Y., & Yu, W. (2017). Formation and variation of the atmospheric heat source over the Tibetan Plateau and its climate effects. *Advances in Atmospheric Sciences*, *34*(10), 1169–1184. https://doi.org/10.1007/s00376-017-7014-5

Wu, G., Liu, Y., He, B., Bao, Q., Duan, A., & Jin, F.-F. (2012). Thermal controls on the Asian summer monsoon. *Scientific Reports*, *2*(1), 404. https://doi.org/10.1038/srep00404

Xu, J., Koldunov, N. V., Remedio, A. R. C., Sein, D. V., Rechid, D., Zhi, X., et al. (2019). Downstream effect of Hengduan Mountains on East China in the REMO regional climate model. *Theoretical and Applied Climatology*, *135*(3–4), 1641–1658. https://doi.org/10.1007/s00704-018-2721-0

Yamazaki, D., Ikeshima, D., Tawatari, R., Yamaguchi, T., O'Loughlin, F., Neal, J. C., et al. (2017). A high-accuracy map of global terrain elevations. *Geophysical Research Letters*, *44*(11), 5844–5853. https://doi.org/10.1002/2017GL072874

Yang, R., Fellin, M. G., Herman, F., Willett, S. D., Wang, W., & Maden, C. (2016). Spatial and temporal pattern of erosion in the three rivers region, southeastern Tibet. *Earth and Planetary Science Letters*, *433*, 10–20. https://doi.org/10.1016/j.epsl.2015.10.032

Yasutomi, N., Hamada, A., & Yatagai, A. (2011). Development of a long-term daily gridded temperature dataset and its application to rain/snow discrimination of daily precipitation. *Global Environmental Research*, 165–172.

Yatagai, A., Kamiguchi, K., Arakawa, O., Hamada, A., Yasutomi, N., & Kitoh, A. (2012). APHRODITE: Constructing a long-term daily gridded precipitation dataset for Asia based on a dense network of rain gauges. *Bulletin of the American Meteorological Society*, *93*(9), 1401–1415. https://doi.org/10.1175/BAMS-D-11-00122.1

Yu, E., Zhang, R., Jiang, D., Ramstein, G., Zhang, Z., & Sun, J. (2018). High-resolution simulation of Asian monsoon response to regional uplift of the Tibetan Plateau with regional climate model nested with global climate model. *Global and Planetary Change*, *169*, 34–47. https://doi.org/10.1016/j.gloplacha.2018.07.002

Zeman, C., Wedi, N. P., Dueben, P. D., Ban, N., & Schär, C. (2021). Model intercomparison of COSMO 5.0 and IFS 45r1 at kilometer-scale grid spacing. *Geoscientific Model Development*, *14*(7), 4617–4639. https://doi.org/10.5194/gmd-14-4617-2021

Zhang, K., Pan, S., Cao, L., Wang, Y., Zhao, Y., & Zhang, W. (2014). Spatial distribution and temporal trends in precipitation extremes over the Hengduan Mountains region, China, from 1961 to 2012. *Quaternary International*, *349*, 346–356. https://doi.org/10.1016/j.quaint.2014.04.050

Zhang, R., Jiang, D., Zhang, Z., & Yu, E. (2015). The impact of regional uplift of the Tibetan Plateau on the Asian monsoon climate. *Palaeogeography, Palaeoclimatology, Palaeoecology*, *417*, 137–150. https://doi.org/10.1016/j.palaeo.2014.10.030

Zhang, Y., Li, T., & Wang, B. (2004). Decadal change of the spring snow depth over the Tibetan Plateau: The associated circulation and influence on the East Asian summer monsoon. *Journal of Climate*, *17*(14), 2780–2793. https://doi.org/10.1175/1520-0442(2004)017⟨2780:DCOTSS⟩2.0.CO;2

Zhang, Z., Chan, J. C. L., & Ding, Y. (2004). Characteristics, evolution and mechanisms of the summer monsoon onset over Southeast Asia. *International Journal of Climatology*, *24*(12), 1461–1482. https://doi.org/10.1002/joc.1082

Zhao, P., & Chen, L. (2001). Climatic features of atmospheric heat source/sink over the Qinghai-Xizang Plateau in 35 years and its relation to rainfall in China. *Science in China - Series D: Earth Sciences*, *44*(9), 858–864. https://doi.org/10.1007/BF02907098

Zhou, T., & Yu, R. (2005). Atmospheric water vapor transport associated with typical anomalous summer rainfall patterns in China. *Journal of Geophysical Research*, *110*(D8), 1–10. https://doi.org/10.1029/2004JD005413

Zhou, W., Tang, J., Wang, X., Wang, S., Niu, X., & Wang, Y. (2016). Evaluation of regional climate simulations over the CORDEX-EA-II domain using the COSMO-CLM model. *Asia-Pacific Journal of Atmospheric Sciences*, *52*(2), 107–127. https://doi.org/10.1007/s13143-016-0013-0

## References From the Supporting Information

Barber, C. B., Dobkin, D. P., & Huhdanpaa, H. (1996). The quickhull algorithm for convex hulls. *ACM Transactions on Mathematical Software*, *22*(4), 469–483. https://doi.org/10.1145/235815.235821

Barnes, R. (2016). RichDEM: Terrain analysis software [Software]. *GitHub*. Retrieved from http://github.com/r-barnes/richdem

Behnel, S., Bradshaw, R., Citro, C., Dalcin, L., Seljebotn, D. S., & Smith, K. (2011). Cython: The best of both worlds. *Computing in Science & Engineering*, *13*(2), 31–39. https://doi.org/10.1109/MCSE.2010.118

Imamovic, A., Schlemmer, L., & Schär, C. (2019). Mountain volume control on deep-convective rain amount during episodes of weak synoptic forcing. *Journal of the Atmospheric Sciences*, *76*(2), 605–626. https://doi.org/10.1175/JAS-D-18-0217.1

Virtanen, P., Gommers, R., Oliphant, T. E., Haberland, M., Reddy, T., Cournapeau, D., et al. (2020). SciPy 1.0: Fundamental algorithms for scientific computing in Python. *Nature Methods*, *17*(3), 261–272. https://doi.org/10.1038/s41592-019-0686-2